https://doi.org/10.5194/essd-2025-826
Preprint. Discussion started: 30 January 2026

Open Access Earth System Science Data Discussions

NZ-BeachTopo30: A national-scale and full-coverage 30 m beach topography dataset for New Zealand reconstructed by fusing ICESat-2 and Sentinel-2

Yuhao Wang[1], Hao Xu[1], Nan Xu[2,3*], Edward Park[4], Xuejiao Hou[5], Jiayi Fang[6], Zhen Zhang[7], Yongjing Mao[8], Huichao Xin[1], Chunpeng Chen[9], Yinxia Cao[10], Yifu Ou[11], Xinyue Gu[12], Wenyu Li[13], Xiaojuan Liu[2,3], Conghong Huang[14], Qingquan Li[2,3,15]

[1]School of Earth Sciences and Engineering, Hohai University, Nanjing 210098, China
[2]Key Laboratory for Geo-Environmental Monitoring of Great Bay Area, Ministry of Natural Resources, Guangdong Key Laboratory of Urban Informatics & Shenzhen Key Laboratory of Spatial Smart Sensing and Service, Shenzhen University, Shenzhen 518060, China
[3]School of Architecture and Urban Planning, Shenzhen University, Shenzhen 518060, China
[4]National Institute of Education, Earth Observatory of Singapore and Asian School of the Environment, Nanyang Technological University, Singapore.
[5]School of Geospatial Engineering and Science, Sun Yat-Sen University, Guangzhou, China.
[6]Institute of Remote Sensing and Earth Sciences, Hangzhou Normal University, Hangzhou, 311121, China.
[7]Department of Earth and Environmental Sciences, Tulane University, New Orleans, LA, 70118, USA.
[8]Water Research Laboratory, School of Civil and Environmental Engineering, UNSW Sydney, Australia.
[9]State Key Laboratory of Estuarine and Coastal Research, East China Normal University, Shanghai 200241, China.
[10]State Key Laboratory of Resources and Environmental Information System, Institute of Geographic Sciences and Natural Resources Research, Chinese Academy of Sciences, Beijing 100101, China.
[11]School of Energy, Geoscience, Infrastructure and Society, Heriot-Watt University, Edinburgh, UK.
[12]Department of Land Surveying and Geo-Informatics, Hong Kong Polytechnic University, 11 Yuk Choi Rd, Hung Hom, Hong Kong, China.
[13]Department of Geography and Planning, University of Toronto, Toronto, ON M5S 3G3, Canada.
[14]College of Land Management, Nanjing Agricultural University, Nanjing, 210095, China
[15]Guangdong Laboratory of Artificial Intelligence and Digital Economy (SZ), Shenzhen 518107, China

Correspondence to: N. Xu (xunan2025@szu.edu.cn)

Abstract. Beaches provide essential ecological functions and support socio-economic resilience, yet accurate mapping is hindered by systematic limitations in global Digital Elevation Models (DEMs). A critical challenge remains in the intertidal zone, where frequent tidal inundation creates extensive data voids, disrupting the continuity of coastal topography. To bridge this fundamental data gap, we present NZ-BeachTopo30 which is a national-scale and full-coverage 30 m beach topography dataset for New Zealand constructed by fusing ICESat-2 photon-counting altimetry with Sentinel-2 multispectral time series. Using DeltaDTM as a high-precision baseline for the stable backshore, we trained an XGBoost model on ICESat-2 control points and Sentinel-2 spectral-geometric features to reconstruct the missing intertidal topography specifically. SHAP analysis was further employed to interpret the physical driving mechanisms of these predictors. Validation against airborne Lidar confirmed that the dataset accurately recovers elevations in previously void zones with an RMSE of 0.94 m. By integrating these predictions with the DeltaDTM baseline, the final national-scale product achieves robust accuracy with an R^2 of 0.75

https://doi.org/10.5194/essd-2025-826
Preprint. Discussion started: 30 January 2026

and an RMSE of 1.17 m. This targeted integration significantly expanded valid topographic coverage by 145.8% from 79.9 km² to 196.5 km². It delivers the first spatially continuous and full-coverage beach topography dataset for New Zealand. This product distinguishes itself by seamlessly bridging the critical intertidal gap that disconnects land and sea in existing global datasets. Given the global availability of ICESat-2 and Sentinel-2, NZ-BeachTopo30 offers a scalable solution for worldwide applications and provides a robust foundation for inundation modeling and coastal management.

1 Introduction

Beaches, being among the most widespread types of coastlines, make up about 31% of the world's ice-free shoreline (Luijendijk et al., 2018). Their dynamic changes greatly affect both the natural balance of coastal systems and socio-economic development (Caffyn et al., 2002; Vousdoukas et al., 2020; Zhang et al., 2025). Defined as coastal geomorphic units composed mainly of unconsolidated sediments such as sand and gravel, shaped by waves and longshore currents, beaches are active land-sea interfaces (Li et al., 2022). As a vital part of the world's coastlines, beach systems not only support rich biodiversity and ecological functions but also serve as important natural resources for protecting coastal communities, supporting regional economies, and preserving cultural heritage (Defeo et al., 2021; Nel et al., 2014; Hanley et al., 2014; Li et al., 2022). However, combined pressures from global climate change and growing human activities put these systems at risk of erosion and degradation like never before (Vousdoukas et al., 2020; Luijendijk et al., 2018; Xu and Gong, 2018). Therefore, achieving high-precision, frequent, and large-scale monitoring of beach dynamics, such as elevation, slope, and extent, has become essential for sustainable coastal management, hazard risk evaluation, and ecosystem restoration (Ni et al., 2024; Ma et al., 2023; Meng et al., 2025; Graffin et al., 2025; Turner et al., 2016).

Remote sensing technology provides essential support for the systematic acquisition of beach topographic data (Salameh et al., 2019; Vitousek et al., 2023; Kroon et al., 2007; Xu et al., 2024a; Wang et al., 2025). Airborne and spaceborne Lidar are widely regarded as the "gold standard" because their laser pulses directly generate high-precision three-dimensional point clouds that capture beach microtopography at centimeter-level resolution (Markus et al., 2017; Schmelz and Psuty, 2022; Stockdon et al., 2006). Passive optical techniques offer cost-effective, large-scale and long-term monitoring: stereo-photogrammetry reconstructs elevation from multi-angle imagery but its accuracy drops on homogeneous, low-texture sand (Casella et al., 2020; Burvingt et al., 2025). In contrast, the waterline method derives elevations by pairing time-series images with tidal models yet is unreliable in areas where tide records are sparse (Vos et al., 2019; Xu et al., 2025; Bishop-Taylor et al., 2019). Complementing these approaches, the SWOT mission's near-nadir Ka-band InSAR can now retrieve intertidal topography from a single low-tide pass with mean absolute errors down to 0.13 m (Salameh et al., 2024). In practice, the rapid generation of seamless, country-wide beach elevation products is hindered by the limited, strip-based coverage of lidar, the tide dependence of stereo imaging, and layover constraints on slopes > 1° for SWOT InSAR.

Despite significant recent progress in coastal topographic data acquisition, publicly available datasets still fail to fully characterize beach topography due to systematic limitations (Yao et al., 2025). Mainstream global digital elevation models

https://doi.org/10.5194/essd-2025-826
Preprint. Discussion started: 30 January 2026

such as SRTM and AW3D30 (Farr et al., 2007; Takaku et al., 2016) were primarily designed for inland areas. However, in the intertidal zone, periodic tidal inundation severely interferes with remote sensing signals. As a result, over low-lying sandy coasts, these datasets suffer from both low vertical accuracy and widespread missing values, leaving micro-topographic features and the dynamic behaviour of beach-dune systems unresolved (Zhang et al., 2015; Prakash Mohanty et al., 2020). To address these limitations, several specialized nearshore and coastal topography products have been developed. GLL_DTM_v2 provides a global view of lowland relief but its coarse resolution (~0.01°) renders it unsuitable for characterizing local beach morphology (Vernimmen and Hooijer, 2023). Among high-resolution (~30 m) alternatives, DiluviumDEM and DeltaDTM are prominent global coastal datasets (Dusseau et al., 2023; Pronk et al., 2024). In comparison, DeltaDTM, a coastal-focused product, exhibits superior overall accuracy due to its rigorous integration of satellite altimetry (ICESat-2 and GEDI). For instance, DeltaDTM reports an overall Mean Absolute Error (MAE) of approximately 0.45 m, whereas DiluviumDEM reports a Root Mean Square Error (RMSE) of approximately 1.13m for low-lying coastal areas relevant to sea-level rise scenarios (typically below 2m). However, DeltaDTM's high reliability comes at the cost of spatial continuity, as the complex tidal environment poses a similar challenge. DeltaDTM contains extensive data voids, especially in the low-lying intertidal zones, because strict quality masking is applied to exclude these unstable, tidally affected pixels. Therefore, bridging these systematic data gaps in the intertidal zone through accurate topographic modeling is a critical requirement for complete coastal monitoring.

Here we produced the NZ-BeachTopo30 dataset to bridge the data gap of beach topography in intertidal zones by integrating ICESat-2 satellite laser altimetry with multispectral optical imagery. The dataset retains the high-accuracy DeltaDTM product as a stable baseline for backshore regions while specifically addressing the dynamic intertidal zones where reliable topographic data are absent. A machine learning model was developed to fill these gaps by leveraging high-precision along-track elevation points from ICESat-2 combined with time-series spectral indices and geometric features derived from Sentinel-2 imagery. This model enables pixel-level elevation estimation strictly within the data voids. In this context we explicitly define full coverage as the seamless spatial continuity that spans from the stable backshore dunes down to the lower foreshore. This effectively eliminates the systematic data voids found in conventional DEMs and ensures a complete representation of the beach profile. To our knowledge, NZ-BeachTopo30 represents the first spatially continuous and high-resolution national-scale beach topography dataset for New Zealand. It provides a full-coverage description of the beach surface and offers a new foundation for further applications.

2 Study area and datasets

2.1 Study area

This study focuses on beaches across New Zealand (approximately 166°E–179°E, 34°S–47°S). Located at the tectonic boundary between the Pacific and Australian plates, New Zealand is an island nation with an extensive coastline of approximately 15,000 km (Hamling et al., 2022). Its unique geological setting, combined with wide climatic variation from subtropical to temperate zones, has created highly diverse beach systems, making the country an ideal natural laboratory for

https://doi.org/10.5194/essd-2025-826
Preprint. Discussion started: 30 January 2026

coastal geomorphology research at the national level. Notably, New Zealand's coastal zones are relatively less disturbed by intensive human activities compared to many other populated coastal regions, allowing for the capture of natural beach topographic dynamics with minimal anthropogenic interference. Additionally, the country boasts comprehensive and openly accessible datasets, including high-precision airborne Lidar DEMs (Land Information New Zealand, LINZ), long-term Sentinel-2 satellite imagery, and detailed coastal geographic information (OpenStreetMap, OSM), which provide robust data support for large-scale topographic reconstruction. These beach systems are subject to frequent tidal inundation and periodic exposure driven by dynamic marine processes. Consequently, extensive intertidal zones are formed where the land-sea interface is constantly shifting due to the rise and fall of the tides. In addition, coastal zones in New Zealand are facing growing challenges, including sea-level rise and intensified coastal erosion, underscoring the critical need for accurate, high-resolution topographic reconstruction and monitoring. The study area overview is shown in **Fig.** 1.

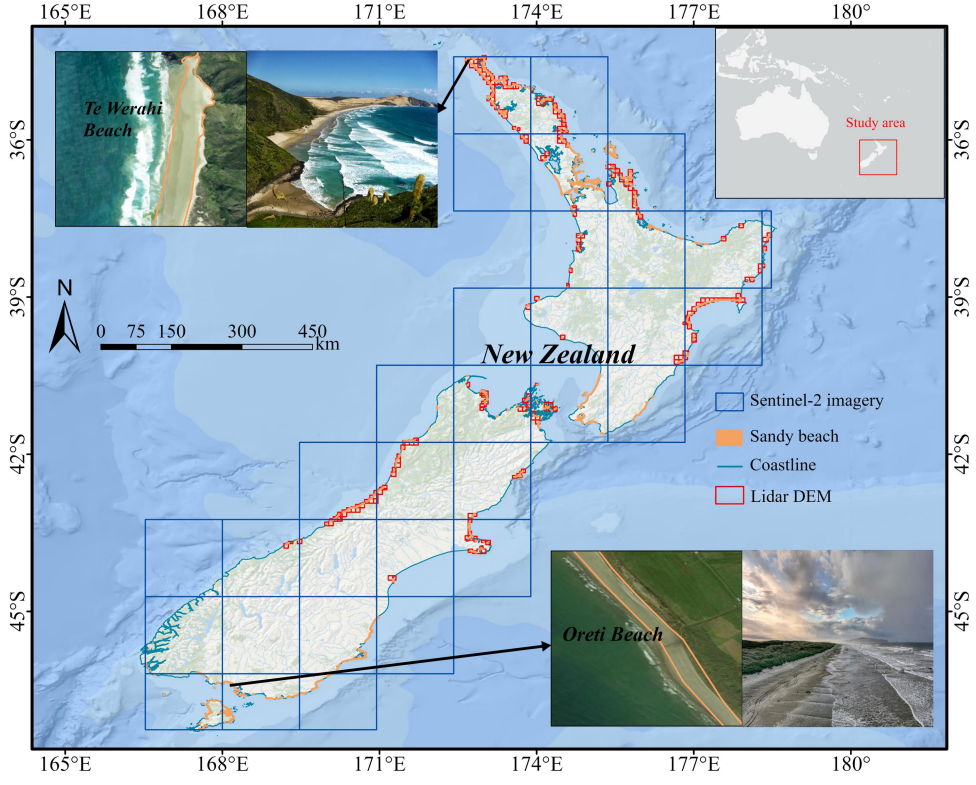

Fig. 1. Geographical information about the study area (New Zealand). The main map displays the spatial distribution of the study datasets: Sentinel-2 image footprints (n = 31; blue boxes), beach polygons (n = 1,713; orange), coastline (cyan lines), and Lidar DEM footprints (n = 309; red boxes). The inset panels, linked by arrows to their corresponding locations, illustrate two representative beaches selected from the North Island (Te Werahi Beach) and South Island (Oreti Beach). In each inset, the left subpanel displays high-resolution satellite imagery of the beach extent, while the right subpanel shows a corresponding field photograph. The background map for the main map and the high-resolution imagery for the insets are World Ocean Base and World Imagery, respectively, both served by Esri via ArcGIS Pro software.

https://doi.org/10.5194/essd-2025-826
Preprint. Discussion started: 30 January 2026

2.2 Topographic datasets

2.2.1 Global public coastal topography product

DeltaDTM is a global Digital Terrain Model (DTM) specifically developed for coastal zones, generated by integrating multi-source remote sensing data including CopernicusDEM, ICESat-2, and GEDI elevation data (Pronk et al., 2024). With a horizontal spatial resolution of 1 arcsecond (~30 m), DeltaDTM provides high vertical accuracy among publicly available global coastal topographic products, achieving an overall mean absolute error (MAE) of 0.45m (Pronk et al., 2024). In this study, DeltaDTM was explicitly selected as the accurate topographic baseline because it prioritizes vertical precision in stable backshore areas, unlike other datasets that often compromise accuracy for broader coverage through interpolation (Pronk et al., 2024). However, to maintain this high reliability, DeltaDTM applies strict quality masking that results in extensive data voids within the intertidal and nearshore shallow-water zones, where tidal variability hinders accurate terrain retrieval (Pronk et al., 2024). These voids often coincide with dynamic beach-face regions that are crucial for coastal morphology analysis. Therefore, the specific purpose of using DeltaDTM in this framework is to serve as an accurate "skeleton" for the dry land. We then employed the machine-learning-predicted elevations to specifically target and fill these missing intertidal and foreshore voids. Through this process, a single, continuous 30 m resolution digital terrain model was generated, seamlessly extending from the backshore dunes to the lower foreshore.

2.2.2 Airborne Lidar DEM

The airborne Lidar data were sourced from LINZ (https://data.linz.govt.nz/layer/121859-new-zealand-lidar-1m-dem/). Acquired via airborne laser scanning, the dataset provides a high-resolution Digital Elevation Model (DEM) with a 1-meter spatial resolution. The data collection period spans from 2018 to 2023, consistent with the acquisition timeline of the optical and laser altimetry satellite data used in this study. The original DEM is referenced to the New Zealand Transverse Mercator 2000 (NZTM2000) coordinate system, with the New Zealand Vertical Datum 2016 serving as the vertical datum. This configuration ensures a vertical accuracy of ±0.2 meters, thereby providing a reliable foundation for precise geospatial analysis in New Zealand's coastal zone. In this study, the high-accuracy Lidar DEM serves as a validation dataset for assessing the accuracy of machine-learning-generated topographic products.

2.3 Satellite remote sensing datasets

2.3.1 Sentinel-2 multispectral imagery

The Sentinel-2 mission, a crucial part of the European Space Agency's Copernicus Program, includes two polar-orbiting satellites (Sentinel-2A and Sentinel-2B) that deliver global multispectral images. This study used the Sentinel-2 Level-2A surface reflectance product, which is atmospherically corrected and suitable for direct surface feature analysis. Sentinel-2 images with less than 10% cloud cover from 2018 to 2023 were selected, resulting in a total of 5942 valid images used for subsequent percentile compositing. The following four spectral bands (at 10 m resolution) were utilized: Blue (B2, 490 nm),

https://doi.org/10.5194/essd-2025-826
Preprint. Discussion started: 30 January 2026

Green (B3, 560 nm), Red (B4, 665 nm), and Near-Infrared (B8, 842 nm). These bands are effective for detecting key beach features (Ni et al., 2024; Wang et al., 2025), including moisture, sediment types, and vegetation, providing vital spectral data for topographic mapping of beaches.

2.3.2 ICESat-2 satellite altimetry data

ICESat-2 (Ice, Cloud, and land Elevation Satellite-2), equipped with the Advanced Topographic Laser Altimeter System (ATLAS), provides high-precision global elevation measurements using photon-counting Lidar technology (Markus et al., 2017; Yao et al., 2024). This study employed the ATL03 Global Geolocated Photon data product, which contains geographic coordinates and elevation values for each detected photon. The data acquisition period spans from the satellite's launch in 2018 to 2023, overlapping with the Sentinel-2 image dates. Photon measurements over beaches along the New Zealand coast were extracted from all relevant satellite tracks to serve as precise elevation control points for the machine learning model.

2.4 Ancillary data

This study also incorporated coastal geographic information from OSM, including coastline, land surface, and beach surface datasets. The coastline data were used to define the land–sea boundary to provide the spatial basis for calculating geometric features. The land surface data were employed to identify terrestrial regions and assist in the generation of coastal buffer zones. The beach surface data were utilized to delineate the spatial extent of beaches and to guide data filtering and model application. Together, these ancillary datasets provided essential geographic context, supporting the accurate identification of beach areas and the quantitative characterization of their spatial attributes.

3 Methodology

To generate the national-scale NZ-BeachTopo30 dataset and effectively bridge the persistent data gap in the intertidal zone, this study implements a specialized data production workflow. This workflow fuses ICESat-2 laser altimetry with Sentinel-2 multispectral imagery. Our approach specifically aims to reconstruct the missing intertidal topography that is currently absent in baseline datasets due to tidal inundation. The overall methodological framework is illustrated in Fig. 2, comprising several key steps: data preprocessing, model training, model validation and interpretation, and model applications.

https://doi.org/10.5194/essd-2025-826
Preprint. Discussion started: 30 January 2026

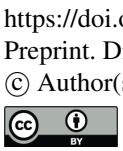

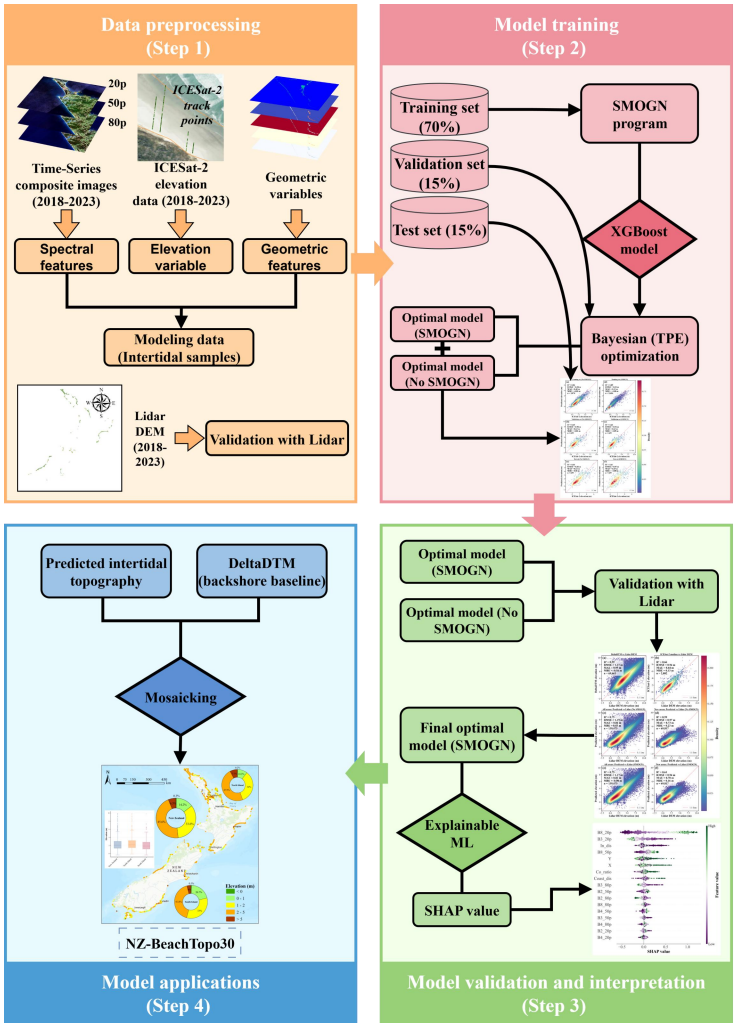

175 **Fig. 2. Workflow used to reconstruct beach topography: (1) Data preprocessing (where 20p, 50p, and 80p refer to the 20th, 50th, and 80th percentile composite images, respectively); (2) Model training; (3) Model validation and interpretation; (4) Model applications.**

3.1. Data preprocessing

3.1.1. Public topographic data preprocessing

180 The DeltaDTM global coastal topography dataset was used as the primary baseline topographic data (Pronk et al., 2024), serving as the high-precision baseline in this study. We aimed to integrate it with our predicted intertidal topography to fill the long-standing intertidal topographic data gaps in this dataset. During the preprocessing stage, only valid DeltaDTM data within the study area were extracted by intersecting with OSM beach polygons, and these valid data were merged into a continuous raster. All spatial extraction and raster merging operations were completed in a Python 3.11 environment.

https://doi.org/10.5194/essd-2025-826
Preprint. Discussion started: 30 January 2026

The 1 m airborne Lidar DEM provided by LINZ served as the validation dataset. Lidar tiles covering the study area and from the 2018-2023 period were selected and mosaicked. The Lidar DEM was then resampled to the 30 m resolution of DeltaDTM. A mean aggregation method was applied during resampling to preserve area-averaged elevation values. To ensure vertical consistency across all topographic products, the Lidar heights were converted from NZVD2016 to orthometric heights referenced to the EGM2008 geoid. This datum transformation was performed in Python 3.11 using the official geodetic models supplied by LINZ, along with the EGM2008 global geoid model.

3.1.2. Preprocessing of Sentinel-2 imagery

Sentinel-2 multispectral imagery preprocessing involved quality control and temporal compositing. First, cloud and cirrus pixels were identified and masked using the Sentinel-2 QA60 band, in which bits 10 and 11 represent cloud and cirrus conditions, respectively. Specifically, pixels with either bit set to 1 were excluded to remove cloud contamination and improve the reliability of subsequent spectral and percentile compositing analyses (Baetens et al., 2019).

Second, we screened out Sentinel-2 images acquired between 2018 and 2023 with scene-level cloud cover below 10% to reduce the influence of clouds and shadows. For each 10 m spectral band, per-pixel 20th-, 50th-, and 80th-percentile values were computed to produce low-, median-, and high-reflectance composite layers. This percentile compositing serves not only as a noise-filtering but also embodies a physical grouping. By aggregating multiple observations across the tidal cycle, the composite layers can effectively capture the reflectance variability caused by tidal inundation, moisture fluctuations, and wave run-up (Chen et al., 2023; Zhang et al., 2022; Zhao et al., 2020; Mao et al., 2021; Wang et al., 2025). Consequently, the low-percentile layer tends to capture conditions of minimal surface reflectance (e.g., wetter, inundated states), whereas the high-percentile layer reflects drier or more exposed states, thereby preserving spectral gradients related to tidal exposure and moisture content (Zhao et al., 2020). All processing was conducted on the Google Earth Engine (GEE) platform, which enabled efficient large-scale computation (Amani et al., 2020).

3.1.3. Preprocessing of ICESat-2 data

The preprocessing of ICESat-2 ATL03 photon returns was specifically designed to extract reliable terrain signals from the complex intertidal environment, including four key steps, i.e., noise removal, smoothing, vertical-datum transformation, and aggregation. First, the official signal-photon identification algorithm associated with the ATL03 product was applied to remove noise. Specifically, photons were screened by the photon confidence flag (signal_conf_ph), and only signal photons with signal_conf_ph ≥ 2 were retained. This step effectively reduced contributions from atmospheric scattering, solar reflections, and instrument noise and improving the along-track signal-to-noise ratio (Lao et al., 2021).

Second, residual outliers were removed while preserving the coherent geomorphic structure of intertidal terrain profiles. This was achieved through an adaptive denoising strategy based on OPTICS clustering. The reachability-distance threshold for this clustering was determined automatically using the Otsu method. Subsequently, a moving-window filter was applied to further suppress non-terrain artifacts, such as vegetation, buildings, and sporadic scatter. Finally, the retained terrain-photon

https://doi.org/10.5194/essd-2025-826
Preprint. Discussion started: 30 January 2026

height series were smoothed using robust locally weighted regression (rLowess). This step reduced high-frequency fluctuations while maintaining the broader morphological trend (Jacoby, 2000).

Third, heights were converted from WGS84 ellipsoidal heights to orthometric heights referenced to the EGM2008 geoid to ensure vertical consistency with other datasets; this vertical-datum transformation followed standard geodetic procedures and was implemented in a Python 3.11 processing environment using the official EGM2008 model (Snyder, 1987). Subsequently, the processed photon points were resampled to the resolution of the DeltaDTM grid. The median photon elevation within each grid cell was calculated, constituting a robust resampling method that further suppressed residual noise from transient water surfaces or scattering. This procedure yielded 4,392 valid ICESat-2 pixels distributed across 340 beaches, accounting for 21.57% of all beach units.

To strictly focus the modeling on the active intertidal and foreshore zones, we excluded cells with median elevations outside the −2 m to 10 m interval. This vertical constraint is specifically aligned with the tidal characteristics of New Zealand. According to Land Information New Zealand (LINZ), the tidal range varies significantly across the country, with an average range of approximately 2 m and maximum ranges reaching up to 3.5 m in specific regions. Therefore, the −2 m lower bound was selected to not only encompass the lowest intertidal zones exposed during spring low tides but also to filter out invalid returns from the surf zone (e.g., extreme wave breaking) or deeper bathymetry.

3.1.4. Other data preprocessing

Other auxiliary datasets were processed to improve spatial consistency, including cleaning and applying spatial masks. Beach-face polygons that did not intersect land or were implausibly far from the coastline (e.g., >1 km) were removed as misclassifications. In addition, beach polygons with an area smaller than a single pixel were excluded because they were smaller than the minimum mapping unit. After these preprocessing steps, a total of 1,576 beach-face polygons were retained for analysis. Since the OSM coastline tracks the mainland and beach polygons reach the low-tide zone, we created a buffered coastline to bridge this gap. We first merged the cleaned beach polygons with the land-area mask to create a combined land mask. The outer boundary of this mask was then converted into a line feature, which we used as the buffered coastline to compute distances from beach pixels to the shoreline.

3.1.5 Feature extraction

To construct the machine learning model, this study extracted and constructed feature samples for training and testing from preprocessed multi-source data. The response variable was the median elevation of ICESat-2 data at the DeltaDTM pixel scale, with the valid range strictly limited to -2 to 10 m to focus on the main beach and active intertidal area. Crucially, samples were only collected from regions where DeltaDTM lacked topography coverage, ensuring the model was trained exclusively to reconstruct the missing intertidal interface.

The spectral features were derived from percentile composites (20th, 50th, and 80th) of four Sentinel-2 bands: Blue (B2), Green (B3), Red (B4), and Near-Infrared (B8). These percentile-based features capture the spectral dynamics under different

https://doi.org/10.5194/essd-2025-826
Preprint. Discussion started: 30 January 2026

tidal and moisture conditions, thereby reducing transient noise and improving the robustness of the topographic inversion (Wang et al., 2025).

Geometric and spatial features included the longitude and latitude of the pixel center (X, Y), the Euclidean distance from the pixel to the coastline, the shortest Euclidean distance to the landward boundary of valid DeltaDTM data, and a standardized relative position index. To account for location variability independent of absolute distance, a standardized relative position index was also computed as follows:

$$P_r = \frac{D_{sea}}{D_{sea}+D_{land}} \quad (1)$$

where P_r represents the relative position, D_{sea} denotes the distance to the sea, and D_{land} represents the distance to the land. This index normalizes the pixel position to the range [0, 1], where smaller values indicate the pixel is closer to the seaward side, and larger values indicate it is closer to the landward side.

These geometric and spatial features collectively provide the model with multi-scale spatial contextual information, ranging from absolute geographic location to relative profile morphology. They effectively constrain the elevation distribution of beach topography and are key for enhancing the model's generalization capability (Xu et al., 2024b; Wang et al., 2025).

The category, name, and description of each input feature are detailed in Table 1.

https://doi.org/10.5194/essd-2025-826
Preprint. Discussion started: 30 January 2026

Table 1. Category, name, and description of input features for beach elevation prediction model.

Feature category	Feature name	Feature description
Spectral features	B2_20p, B2_50p, B2_80p	20th, 50th, and 80th percentiles of the Blue Band (B2)
	B3_20p, B3_50p, B3_80p	20th, 50th, and 80th percentiles of the Green Band (B3)
	B4_20p, B4_50p, B4_80p	20th, 50th, and 80th percentiles of the Red Band (B4)
	B8_20p, B8_50p, B8_80p	20th, 50th, and 80th percentiles of the Near-Infrared Band (B8)
Geometric and spatial features	X, Y	Longitude and latitude coordinates of the pixel center (WGS84 datum)
	D_{sea} (Coast_dis)	Shortest Euclidean distance from the pixel center to the coastline (unit: m)
	D_{land} (In_dis)	Shortest Euclidean distance from the pixel center to the land boundary of DTM data (unit: m)
	P_r (Co_ratio)	Relative position index

3.2 Model training

3.2.1 Sample splitting and balancing strategy

All 12 spectral features and 5 geometric-spatial features of the pixels were matched with corresponding ICESat-2 elevation values, resulting in a total of 4,392 valid samples. The samples were randomly divided into a training set, validation set, and test set, with proportions of 70%, 15%, and 15% respectively. Specifically, the training set (3,074 samples) was used for model parameter learning, the validation set (659 samples) for hyperparameter tuning and early stopping, and the test set (659 samples) for the final evaluation of model generalization performance.

Sample imbalance is a critical issue in regression modeling, as it causes the model to be biased toward data-dense areas. This is particularly common in intertidal topographic modeling, where elevation samples are often concentrated in the mid-

https://doi.org/10.5194/essd-2025-826
Preprint. Discussion started: 30 January 2026

intertidal range near mean sea level (e.g., 2 to 3 m), while samples from the low-lying intertidal (e.g., below 1 m) and subtidal zones (e.g., below 0 m) below sea level are scarce due to the limited observation windows during low tides (He and Garcia, 2009). These sparse samples often correspond to geomorphologically significant zones. Training a model directly on such an imbalanced dataset will cause the algorithm to prioritize prediction accuracy in data-dense intervals at the expense of performance in sparse intervals such as low elevation areas, ultimately leading to systematic biases or reduced accuracy in topographic products for critical foreshore and subtidal slopes.

To address this issue, this study employed the Synthetic Minority Over-Sampling with Gaussian Noise (SMOGN) algorithm for data balancing (Branco et al., 2017), applying it exclusively to the training set. SMOGN is an improved method based on the Synthetic Minority Over-sampling Technique (SMOTE) (Chawla et al., 2002), which combines over-sampling and under-sampling strategies to generate synthetic samples consistent with the original data distribution while avoiding the overfitting risk of traditional SMOTE in ambiguous boundary regions. This strategy ensures the model receives balanced learning signals across all elevation intervals while preserving the original distribution of the validation and test sets, enabling objective evaluation of generalization capability. The core mechanism of the SMOGN algorithm is as follows: first, it identifies the k-nearest neighbors of each minority-class sample using Euclidean distance; for samples in "safe regions" (most neighbors belong to the minority class), it adopts a strategy similar to SMOTE and generates synthetic samples via random linear interpolation (Chawla et al., 2002); for samples in "dangerous regions" (approximately half of the neighbors belong to the majority class), it first generates synthetic samples via SMOTE interpolation and then adds moderate Gaussian noise to these interpolated samples, enhancing robustness in ambiguous boundary areas; for "outlier regions" (most neighbors belong to the majority class), it avoids generating synthetic samples to prevent reinforcing noise. Simultaneously, it performs under-sampling by removing Tomek links from the majority class to eliminate ambiguous overlaps between classes. This combined strategy effectively balances data distribution while preserving the statistical properties and structure of the original dataset. It has been proven in various remote sensing applications to improve prediction accuracy and robustness in data-sparse regions (Wen et al., 2024).

In this study, the SMOGN algorithm was implemented using the smogn package in Python 3.11 and applied exclusively to the training set. In this process, ICESat-2 elevation was used as the response variable, and the target range for balancing was set to [-2, 10] m, to ensure the focus remained strictly on the active intertidal domain. Key parameter settings were as follows: number of neighbors k = 5 (to ensure local plausibility of synthetic samples), sampling mode set to "extreme" (focusing on extreme values at both ends of the distribution), relative threshold of 0.7 (to identify minority samples requiring prioritized processing), anomaly detection method "auto" (to automatically identify high and low elevation extreme anomalies), relative extreme type "both" (to address imbalance at both high and low elevation ends), relative coefficient of 1.2 (to appropriately expand the processing range for extreme samples), and Gaussian noise perturbation amplitude of 0.01 (to ensure diversity and rationality of synthetic samples). Based on preliminary experiments, this parameter combination was confirmed to effectively balance the sample distribution across different elevation intervals in the training set while preserving the statistical characteristics of the original data.

https://doi.org/10.5194/essd-2025-826
Preprint. Discussion started: 30 January 2026

3.2.2 XGBoost configuration and hyperparameter optimization

This study adopted the eXtreme Gradient Boosting (XGBoost) algorithm for beach elevation prediction (Chen and Guestrin, 2016). XGBoost is particularly well-suited for modeling nonlinear relationships in structured, tabular data and offers several advantages over deep learning alternatives for this specific application (Shwartz-Ziv and Armon, 2022). First, it achieves high predictive accuracy with significantly lower computational cost and training time, which is crucial when processing large-scale geographic datasets (Shwartz-Ziv and Armon, 2022). Second, XGBoost demonstrates strong robustness to overfitting even with moderate sample sizes, making it ideal for our dataset of 4,392 ICESat-2 elevation samples. Third, the tree-based architecture provides inherent feature importance scores that yield physically interpretable insights into how spectral and geometric features influence elevation predictions, whereas deep neural networks remain difficult to interpret (Lundberg et al., 2020). While Convolutional Neural Networks and other deep learning models excel at extracting patterns from raw imagery, they are less effective for the engineered feature set used here, namely, percentile composites and distance metrics (Shwartz-Ziv and Armon, 2022). In addition, deep learning would require substantially larger training datasets and computational resources without commensurate accuracy gains for this structured data problem (Shwartz-Ziv and Armon, 2022). Therefore, XGBoost represents the optimal balance of predictive performance, computational efficiency, and model interpretability for fusing multisource remote sensing features to reconstruct beach topography (Ye et al., 2024). A global model training strategy was employed without regional partitioning, and model optimization was completed through a systematic Bayesian hyperparameter tuning framework.

In the data preprocessing stage, both features and the target variable (elevation) in the training set were standardized to have a mean of 0 and a standard deviation of 1. This operation ensured that all input variables were on a comparable scale, laying the foundation for stable and efficient model convergence.

For hyperparameter optimization, we used the Tree-structured Parzen Estimator (TPE) Bayesian optimization algorithm implemented in the Optuna library (Wang and Sherry Ni, 2019). This algorithm can iteratively build a probabilistic model of the objective function based on prior trial results, efficiently searching the predefined hyperparameter space. The optimization objective was set to the RMSE of the validation set to identify the optimal parameter combination.

To address the imbalance in elevation sample distribution, the SMOGN algorithm was exclusively applied to the training set. The validation set and test set retained their original data distributions to ensure the objectivity of the evaluation of model generalization ability and avoid evaluation bias caused by changes in data distribution.

An early-stopping mechanism was integrated into the training process, with a patience of 50 epochs. After each training round, the RMSE of the validation set was evaluated. When no improvement in the validation set RMSE was observed for 50 consecutive rounds, the training was terminated, and the model state from the epoch with the best validation performance was retained. This effectively prevented model overfitting and reduced unnecessary computational cost.

Models were trained separately on the original imbalanced data and the SMOGN-balanced data. Finally, the generalization performance of the two types of models was comprehensively evaluated using an independent test set to determine the optimal

https://doi.org/10.5194/essd-2025-826
Preprint. Discussion started: 30 January 2026

model suitable for this study. Table 2 presents the search ranges of XGBoost hyperparameters and their optimal values before and after data balancing, providing key parameter support for the model training process.

Table 2. Search ranges and optimal values of XGBoost hyperparameters (before and after SMOGN balancing)

Hyperparameter	Search range	Optimal value (before SMOGN)	Optimal value (after SMOGN)
n_estimators	200 – 600 (integer)	565	401
max_depth	2 – 6 (integer)	5	4
learning_rate	0.001 – 0.2 (float, log-scaled)	0.083	0.199
subsample	0.5 – 1.0 (float)	0.680	0.849
colsample_bytree	0.5 – 1.0 (float)	0.781	0.674
reg_alpha (L1)	1.0 – 50.0 (float)	3.404	1.925
reg_lambda (L2)	10.0 – 100.0 (float)	14.690	54.263
gamma	0.1 – 2.0 (float)	0.134	0.172
min_child_weight	1 – 50 (integer)	16	1

3.3 Model validation and interpretation

A comprehensive evaluation framework was established to assess both the predictive behavior of the machine learning model and the accuracy of the final applied beach topography. The first part of the evaluation focused on point-level predictive performance using the ICESat-2 median elevation samples. Independent training, validation, and test datasets were used to quantify the model's learning and generalization behavior. The second part was a comprehensive accuracy validation of the results of this study based on the Lidar DEM, which includes point-level accuracy validation, profile and spatial accuracy validation (assessed at 6 beaches), and cross-beach transferability validation. To quantify accuracy, this study employed four metrics, namely the coefficient of determination (R^2), RMSE, MAE, and mean bias error (MBE). Their calculation formulas are provided as follows.

$$R^2 = 1 - \frac{\sum_{i=1}^{n}(y_i - \hat{y}_i)^2}{\sum_{i=1}^{n}(y_i - \bar{y})^2} \quad (2)$$

$$RMSE = \sqrt{\frac{1}{n}\sum_{i=1}^{n}(y_i - \hat{y}_i)^2} \quad (3)$$

$$MAE = \frac{1}{n}\sum_{i=1}^{n}|y_i - \hat{y}_i| \quad (4)$$

$$MBE = \frac{1}{n}\sum_{i=1}^{n}(y_i - \hat{y}_i) \quad (5)$$

among these variables, y_i represents the measured elevation value from ICESat-2, $\hat{y}_i$ denotes the model-predicted elevation value, $\bar{y}$ is the average of the measured values, and n stands for the number of samples. By comparing these metrics across the

https://doi.org/10.5194/essd-2025-826
Preprint. Discussion started: 30 January 2026

training set (reflecting model fit), validation set (reflecting model tuning effectiveness), and test set (reflecting model generalization), we can systematically diagnose whether the model suffers from overfitting or underfitting and confirm its robustness.

To ensure the representativeness and validity of profile and spatial accuracy validation, the 6 random beaches used in this process were selected by stratifying New Zealand's North and South Islands (3 each) to cover coastal topographic diversity, with strict requirements for complete airborne Lidar DEM coverage to enable high-precision reference comparison and sufficient predicted pixels to focus on the study's core supplemented topography. The detailed information of these 6 beaches is shown in Table 3.

Table 3. Detailed information of the 6 randomly selected beaches for validation

Beach FID	Geographic location (island)	Proportion of predicted pixels.
220	South island	54.1%
222	South island	75.9%
678	South island	31.7%
343	North island	35.2%
418	North island	63.5%
421	North island	39.6%

To interpret the predictions of the optimized XGBoost model and to quantify the relative importance of input variables in predicting beach elevation, we employed the SHAP (SHapley Additive exPlanations) framework (Lundberg, 2017). SHAP is a framework derived from cooperative game theory that attributes each model prediction to the contribution of individual input features by distributing the prediction value among them in a theoretically consistent manner. This method provides an intuitive and model-agnostic approach for understanding how different features influence the predictions.

In this study, SHAP values were calculated using all samples from the independent test dataset, which had not been used during model training. The SHAP computation was carried out in Python 3.11 using the TreeExplainer algorithm, which is specifically designed for tree-based ensemble models such as XGBoost. This procedure provides a transparent and data-driven interpretation of how spectral and geometric features influence beach elevation predictions.

3.4 Model applications

The goal of this study is to generate a seamless national-scale beach topographic product by effectively bridging the persistent data gaps in the existing baseline. To achieve this, a targeted fusion strategy was adopted that integrates the high-precision backshore topography from DeltaDTM with our reconstructed intertidal topography.

The specific workflow involved two main stages. First, the preprocessed Sentinel-2 spectral features and geometric features (17 in total) covering the national beach areas were input into the trained and optimized XGBoost model. This step focused specifically on the regions identified as "NoData" in DeltaDTM and generated pixel-level elevation predictions exclusively

https://doi.org/10.5194/essd-2025-826
Preprint. Discussion started: 30 January 2026

for the missing intertidal and foreshore zones. Second, these predicted elevations were seamlessly mosaicked with the valid DeltaDTM pixels. By treating DeltaDTM as the accurate "skeleton" for stable terrain and the ML predictions as the "connective tissue" for dynamic zones, yielding a single, continuous 30 m resolution digital terrain model. The final product extends from the backshore dunes to the underwater shoreface without altering the verified high-quality data in the baseline. Ultimately, a complete, continuous, and seamless digital terrain model spanning from the backshore to the underwater shoreface is formed.

4 Results

4.1 Model performance

Data balancing with the SMOGN algorithm effectively reduced systematic overestimation of low-elevation values and improved the overall distribution of predicted beach elevations (Fig. 3(a)-(f)). Before data balancing (Fig. 3(a)-(c)), the model tended to overpredict near-zero elevations, as reflected in the validation and test sets. In the test set, the mean bias error (MBE) reached 0.06 m, indicating a slight but consistent overestimation. After applying SMOGN (Fig. 3(d)–(f)), the number of training samples increased from 3,074 to 5,606, expanding the model's capacity to capture low-elevation cases. Consequently, the test-set MBE decreased from 0.06 m to 0.00 m, confirming that the average bias was effectively corrected. The balanced model also produced predictions with a wider and uniform range, indicating improved representation of elevation variability across coastal zones.

Model accuracy remained satisfactory after balancing, maintaining sub-meter accuracy (i.e., RMSE) for both validation and test sets (Fig. 3(d)-(f)). Although the pre-balancing model achieved slightly better accuracy metrics, the balanced version yielded a more uniform distribution of predicted elevations and a more realistic depiction of terrain gradients. This trade-off slightly reduced precision but enhanced spatial consistency, which is preferable for regional-scale coastal terrain modeling. Given the sub-meter RMSE accuracy and the reduced prediction bias, the final model demonstrates strong practical utility for coastal terrain estimation in low-relief environments.

https://doi.org/10.5194/essd-2025-826
Preprint. Discussion started: 30 January 2026

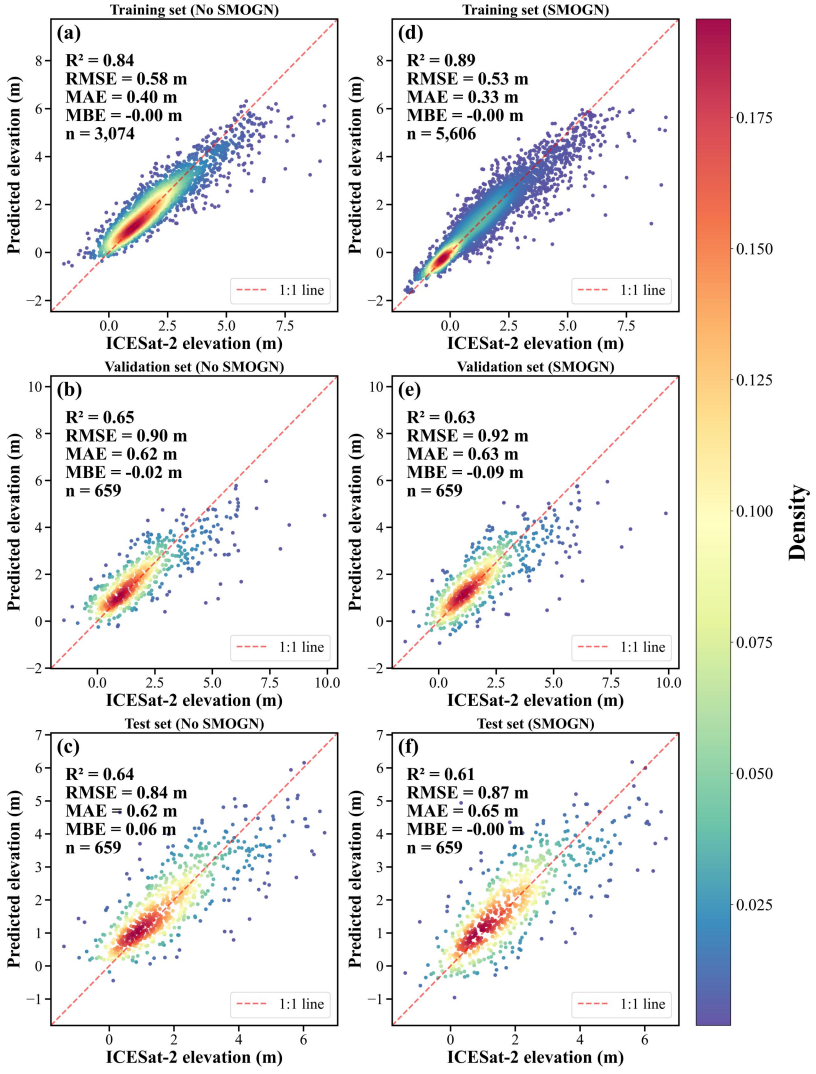

Fig. 3. Predicted versus ICESat-2 elevation scatter plots for the training, validation, and test sets (a-c) before and (d-f) after data balancing. The dot's color ranges from light pink to dark blue, indicating low to high density.

4.2 Accuracy assessment using Lidar DEM

Comparison with airborne Lidar reveals that DeltaDTM systematically underestimates terrain elevation, particularly in low-lying coastal zones (baseline comparison, Fig. 4(a)). Relative to the Lidar DEM, DeltaDTM attains $R^2 = 0.59$, RMSE = 1.37 m, MAE = 0.95 m, and MBE = −0.16 m (Fig. 4(a)). Its elevations are mainly concentrated between 2 m and 6 m, indicating substantial data gaps in low-relief intertidal areas. In contrast, the ICESat-2 median values (overall range: -2 m to 10 m) show good agreement with Lidar but exhibit a positive bias (MBE = 0.13 m) that may propagate into subsequent modeling, with overall metrics of $R^2 = 0.66$, RMSE = 0.94 m, and MAE = 0.64 m.

https://doi.org/10.5194/essd-2025-826
Preprint. Discussion started: 30 January 2026

To validate model performance in these data-void regions, accuracy was first evaluated specifically within the newly supplemented intertidal zones (Fig. 4f). Here, the SMOGN-balanced model achieved an RMSE of 0.94 m and an MAE of 0.70 m. This sub-meter accuracy confirms its capability to reconstruct topography in areas entirely absent from the baseline dataset. Prior to balancing, the model exhibited a positive bias (MBE = 0.23 m; Fig. 4d) in these regions, which was reduced to 0.16 m by the SMOGN algorithm.The final integrated product demonstrates robust overall accuracy. Across the entire study area (Fig. 4e), it attains $R^2 = 0.75$, RMSE = 1.17 m, MAE = 0.82 m, and MBE $\approx$ 0 m. The close agreement between the newly predicted intertidal elevations and the baseline DeltaDTM backshore confirms a seamless integration. While the unbalanced model showed marginally higher scores on some metrics (Fig. 4c), the balanced model delivered more realistic terrain gradients and a smoother cross-shore transition.

Case studies at six beaches show that predicted spatial patterns match realistic coastal morphology, and their aggregated accuracy closely reflects overall model performance (Fig. 5). Pixel-level predictions (Fig. 5a – f) exhibit the expected inland-rising elevation gradients. Aggregated validation against Lidar across all six beaches (n = 16,342 pixels) yields $R^2 = 0.826$, RMSE = 1.054 m, MAE = 0.744 m, and MBE = 0.186 m (Fig. 5g). The slightly positive MBE indicates regional variability, with some beaches showing localized overestimation. Residual analyses for individual beaches reveal location-dependent biases, though most pixel residuals are centered near zero (Fig. 6). The mean residuals for panels (a–f) are −0.182 m, +0.111 m, −0.240 m, +0.132 m, +0.637 m, and −0.077 m, respectively (Fig. 6). The highest mean deviation is observed in panel (e) (+0.637 m), and the smallest absolute bias in panel (f) (−0.077 m). Although minor beach-specific biases exist, most residuals cluster tightly around zero. This demonstrates that the model is largely unbiased at the pixel scale, with any systematic bias confined to specific localities. To validate the vertical gradient consistency of the dataset, we extracted cross-shore profiles perpendicular to the coastline for six representative beaches (FIDs 220, 222, 678, 343, 418, and 421). We conducted pixel-level elevation comparisons between NZ-BeachTopo30 and the Lidar DEM along these profiles as shown in Fig. 7(g)–(l). To focus the assessment on the active beach zone, the comparison was strictly limited to elevation values ranging from -2 m to 10 m. Crucially, the gray-shaded regions in the profile plots highlight the newly added areas, allowing for a targeted evaluation of the gap-filling performance. RMSE and MBE were calculated for each profile to quantify the agreement between the datasets. Among the six beaches, the profile for the beach with FID 222 (Fig. 7(h)) exhibits the highest agreement with the Lidar DEM, achieving an RMSE of 0.421 m and an MBE of -0.139 m (n = 15). The predicted elevation curve closely overlays the Lidar-derived curve, maintaining high consistency even within the newly filled intertidal segment. In contrast, the beach with FID 678 (Fig. 7(i)) shows the lowest profile accuracy, with an RMSE of 1.069 m and an MBE of 0.381 m (n = 9). Although the predicted profile exhibits a positive bias in this specific case, the overall rising trend still aligns with the Lidar reference. For the updated profiles of FID 418 (Fig. 7(k)) and FID 421 (Fig. 7(l)), the model also demonstrates robust performance, yielding RMSE values of 0.502 m and 0.771 m, respectively. Overall, the average RMSE across all six profiles is approximately 0.71 m, indicating that the model effectively captures the cross-shore morphological gradients and successfully reconstructs the topography in the previously missing intertidal zones.

https://doi.org/10.5194/essd-2025-826
Preprint. Discussion started: 30 January 2026

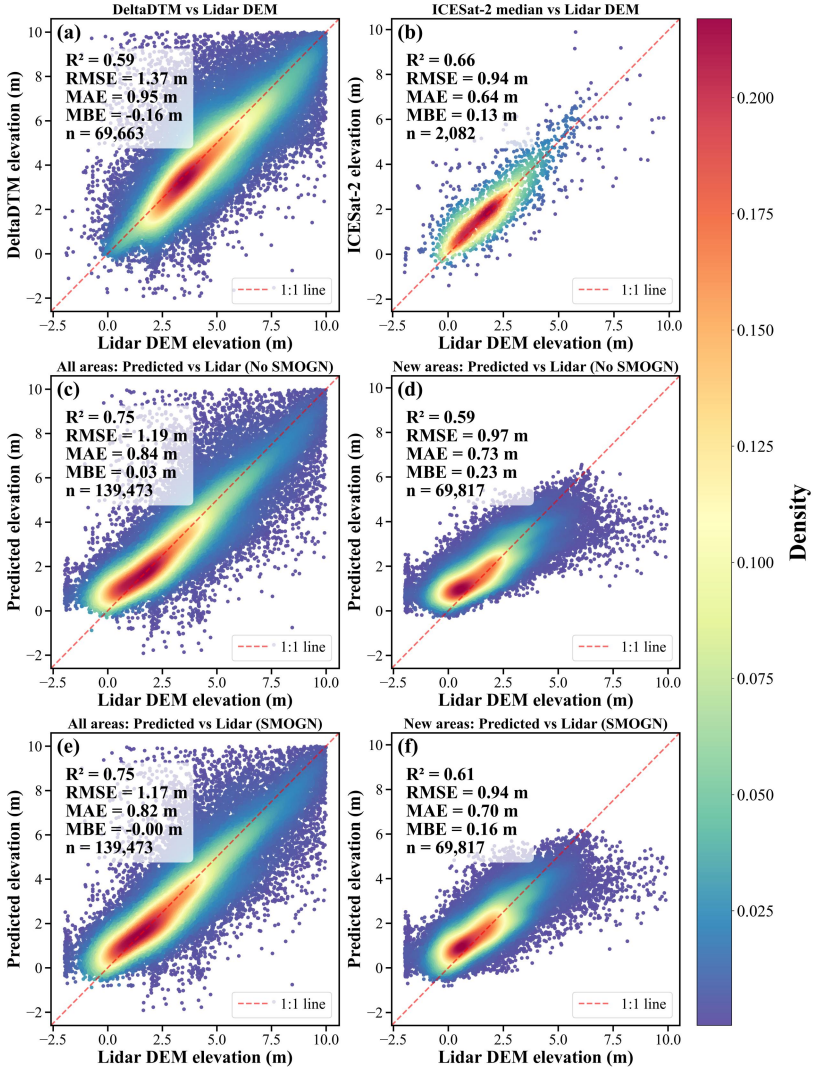

Fig. 4. Density scatter plots for accuracy validation against the Lidar DEM. (a) DeltaDTM versus Lidar DEM; (b) ICESat-2 median values versus Lidar DEM; (c–d) validation of the topography before data balancing for (c) the entire area and (d) the newly supplemented areas; (e–f) validation after data balancing for (e) the entire area and (f) the newly supplemented areas. Dot color from light pink to dark blue represents increasing point density.

https://doi.org/10.5194/essd-2025-826
Preprint. Discussion started: 30 January 2026

Open Access Earth System Science Data Discussions

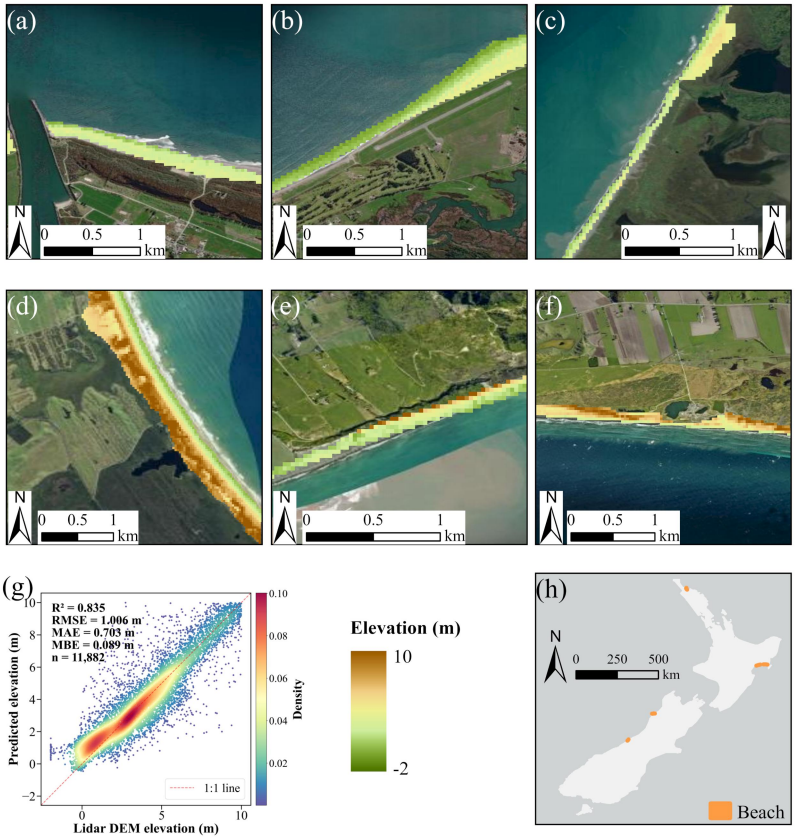

455 **Fig. 5. Topography from the NZ-BeachTopo30 dataset (a)-(f), aggregated validation (g), and geographical context (h) for the six beaches in the study area. The FIDs of the beach polygons in (a)-(f) are 220, 222, 678, 343, 418, and 421, respectively. The background maps for subplots (a)–(f) and (h) are World Imagery and Light Gray Canvas, respectively, both served by Esri via ArcGIS Pro software.**

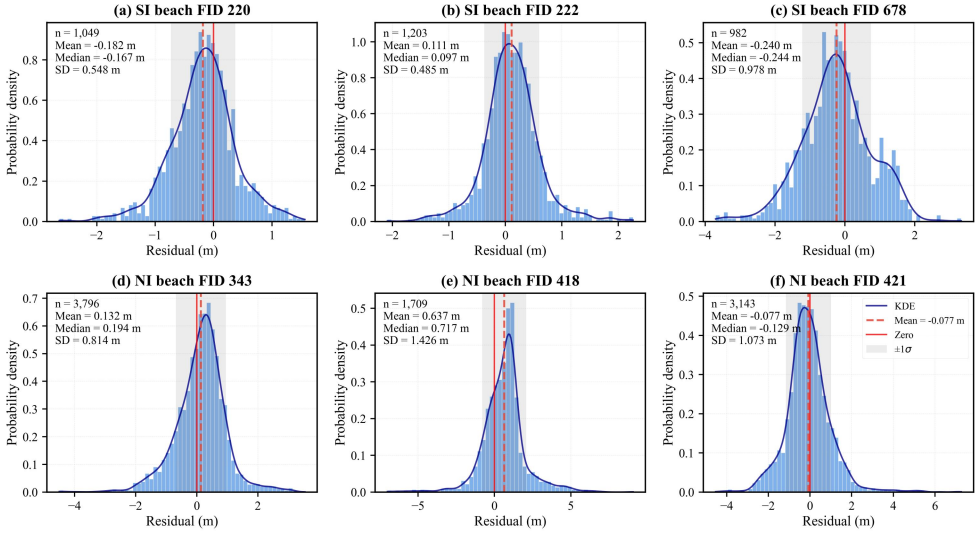

https://doi.org/10.5194/essd-2025-826
Preprint. Discussion started: 30 January 2026

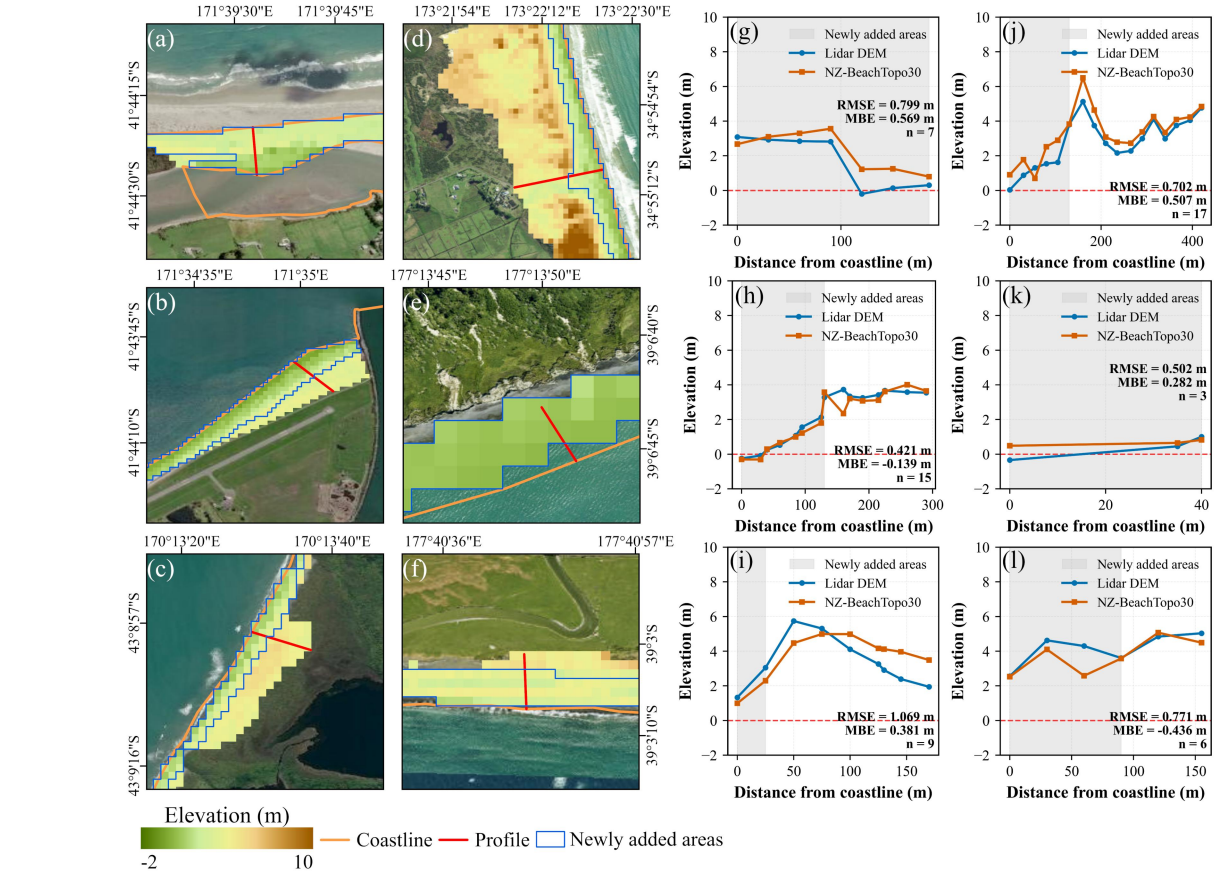

Fig. 6. Residual distributions of the predicted elevation for the six beaches. The legend displayed in (f) is shared across all panels (a)–(f).

Fig. 7. Comparison results of profiles along six beaches. (a)–(f) Geographical locations of the profiles, where the orange line represents the coastline, the red line denotes the profile transect, and the blue polygons indicate the newly added coverage areas. (g)–(l) Cross-shore profiles starting from the coastline, with the blue line indicating results derived from the Lidar DEM and the orange line representing results derived from NZ-BeachTopo30. The gray shaded background highlights the extent of the newly added intertidal areas. The accuracy metrics comparing the results of this study with the Lidar DEM are displayed in the bottom right corner of each plot. Specifically, (a)–(f) and (g)–(l) correspond to beaches with FID 220, 222, 678, 343, 418, and 421, respectively. The background maps for subplots (a)–(f) are World Imagery, served by Esri via ArcGIS Pro software.

4.3 Quantifying the expansion of intertidal beach topography coverage

Our analysis reveals realistic elevation patterns across beach units, with mean-elevation classes concentrated in mid-range intervals (summary by beach polygon, Fig. 8). When mean elevation is classified into five categories (< 0 m, 0-1 m, 1-2 m, 2-5 m, > 5 m), statistical analysis reveals clear spatial variability in beach quantity proportions between New Zealand's North and South Islands, as well as consistent trends at the national scale. Nationally, mid-elevation beaches (1-2 m and 2-5 m) dominate the distribution, while low-elevation beaches (< 0 m and 0-1 m) are relatively scarce, and high-elevation beaches (> 5 m) account for the smallest share. The North Island shows a higher concentration of mid-to-high elevation beaches, whereas

https://doi.org/10.5194/essd-2025-826
Preprint. Discussion started: 30 January 2026

the South Island has a relatively larger proportion of low-elevation beaches, particularly in the 0-1 m interval, which reflects distinct topographic characteristics between the two islands. The inset boxplot in Fig. 8 further quantifies elevation distribution differences: the North Island's beach mean elevations are slightly higher than the South Island's, and the national median mean elevation clusters near 2 m, with the minimum elevation reaching approximately −1 m. This elevation pattern aligns well with the comparison results referenced in Fig. 4(e), which exhibits a notable increase in low-elevation pixels (< 2 m). This consistency confirms that the model successfully reconstructs nearshore intertidal topography. The greater representation of low elevations in NZ-BeachTopo30 directly corresponds to these previously unrecorded intertidal zones, thereby filling the critical data gaps.

Systematic data gaps in coastal DTMs are predominantly concentrated in intertidal zones, where periodic tidal inundation masks low-elevation terrain from conventional sensors (Bishop-Taylor et al., 2019). To quantify the extent of coverage expansion and rigorously demonstrate the full-coverage advantage of NZ-BeachTopo30, we compared the spatial completeness of the baseline DeltaDTM against NZ-BeachTopo30. After projecting both datasets into the NZTM2000 coordinate system, Fig. 9(b) reveals a substantial expansion in coverage: the original DeltaDTM covers only 79.9 km², whereas the mosaicked DeltaDTM expands to 196.5 km². This adds approximately 152,935 new pixels, corresponding to an area of 116.6 km²—a 145.8% increase over the baseline. Furthermore, Fig. 9a indicates that the number of covered beach units increased by 19.5%, from 1,319 to 1,576.

Fig. 9c compares the elevation distributions of the original DeltaDTM and the newly added pixels. The median elevation of the newly added pixels (~1.5 m) is substantially lower than that of the original DeltaDTM (~4 m). The first and third quartiles of the newly added pixels are concentrated at lower elevations, indicating that the model primarily fills gaps in low-elevation areas such as intertidal zones rather than in high-elevation areas. The interquartile range of the newly filled pixels is relatively narrow, which implies that these newly added values are clustered within the low-elevation segment.

Fig. 9d compares the elevation histograms of the original DeltaDTM and the NZ-BeachTopo30 dataset. It shows a substantial increase in the total number of valid pixels after mosaicking, along with a marked increase in the low-elevation range. This pattern indicates that the model effectively predicted missing elevations in nearshore and intertidal zones, thereby improving data continuity in previously missing areas. While the high-elevation portion of the distribution remains largely unchanged, the low-elevation portion exhibits a distinct shift and broadening, reflecting the successful filling of low-lying gaps during the fusion process. Fig. 10(a) illustrates the expansion in beach coverage at the beach-unit level. Beaches already covered by the original DeltaDTM are depicted in green, while those newly covered by the dataset are shown in red. The inset donut chart quantifies this relationship where 83.7% of beach units had prior coverage in DeltaDTM whereas NZ-BeachTopo30 successfully introduced coverage to the remaining 16.3% of beaches that were previously unmapped. Fig. 10(b) further maps the magnitude of these intertidal supplements for individual beaches, classifying each beach into one of four bins based on the size of its newly added area. The inset donut chart presents the frequency distribution of beaches across these size classes. The results reveal that the majority of beaches (56.6%) received only minor area supplements (0–0.01 km²), indicating that for most coastal units, the reconstruction primarily filled narrow intertidal fringes or small voids. However, a notable

https://doi.org/10.5194/essd-2025-826
Preprint. Discussion started: 30 January 2026

Open Access Earth System Science Data Discussions

proportion (15.2%) of beaches gained substantial area coverage (> 0.1 km²). This distribution suggests that while the gap-filling effect is ubiquitous across all beaches, our method is particularly vital for capturing the large intertidal zones of major beach systems that were largely absent from the baseline.

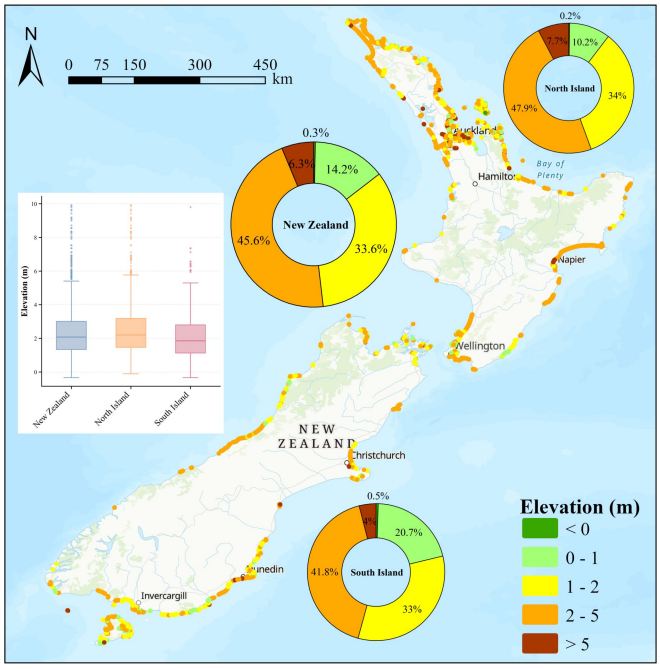

Fig. 8. Spatial distribution and proportional composition of mean beach elevation per polygon. Map shows the geographic location of beach polygons colored by mean elevation interval: below 0 m, 0 to 1 m, 1 to 2 m, 2 to 5 m, and above 5 m. The inset boxplot compares the distribution of beach mean elevations for New Zealand, the North Island, and the South Island. The donut charts report area proportions by elevation interval for New Zealand and for each island; colors in the donuts correspond directly to the map legend. The background map is World Topographic Map, served by Esri via ArcGIS Pro software.

https://doi.org/10.5194/essd-2025-826
Preprint. Discussion started: 30 January 2026

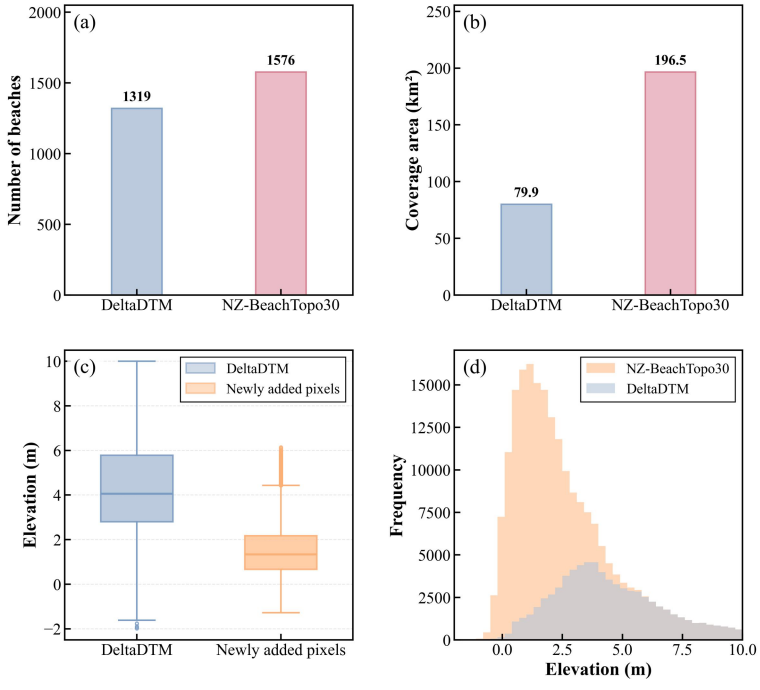

Fig. 9. Impact of data fusion on beach coverage and elevation distribution. (a) Number of beaches covered by the DeltaDTM and NZ-BeachTopo30. (b) Spatial coverage area of the DeltaDTM and NZ-BeachTopo30. (c) Boxplot comparison of elevation distributions between the DeltaDTM and the newly added pixels. (d) Combined elevation histogram showing distributions of the DeltaDTM and NZ-BeachTopo30.

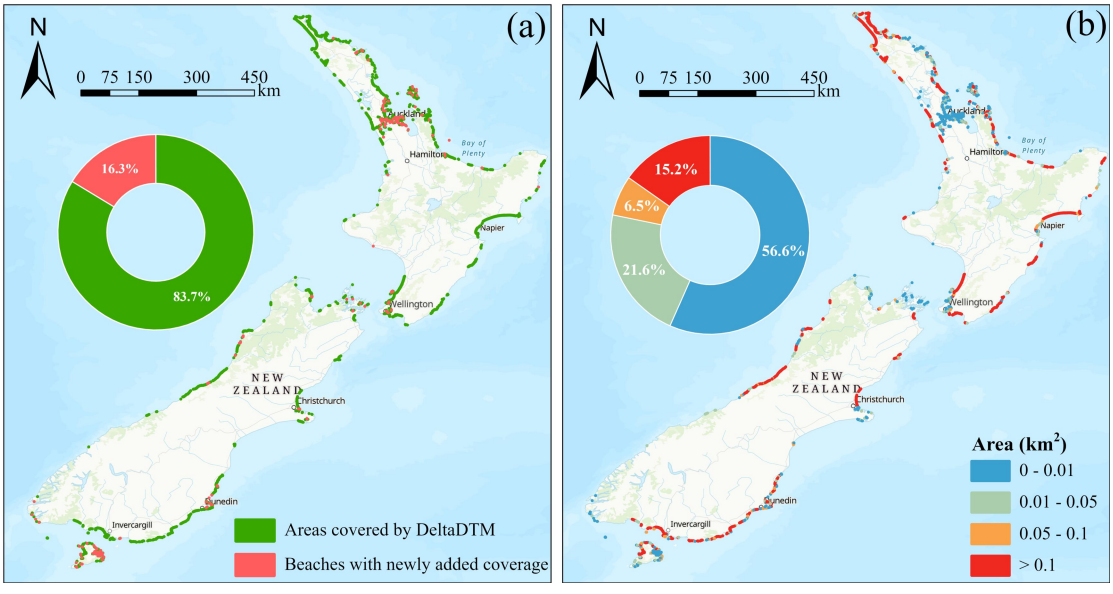

Fig. 10. Spatial distribution and magnitude of the newly supplemented intertidal coverage. (a) Classification of beaches based on original availability: beaches with existing DeltaDTM coverage are shown in green, while beaches newly covered by NZ-BeachTopo30 are shown in red. The inset donut chart indicates that 16.3% of the beach units are newly covered. (b) Spatial distribution of the newly added area magnitude per beach, classified by area bins. The inset donut chart shows the percentage of

https://doi.org/10.5194/essd-2025-826
Preprint. Discussion started: 30 January 2026

beach units falling into each newly added area interval: 0 to 0.01 km² (56.6%), 0.01 to 0.05 km² (21.6%), 0.05 to 0.1 km² (6.5%), and greater than 0.1 km² (15.2%). The background map for panels (a) and (b) is World Topographic Map, served by Esri via ArcGIS Pro software.

4.4 Model transferability across beaches

To evaluate the spatial transferability of the model to beaches without direct ICESat-2 coverage, a comparative accuracy assessment was conducted at the beach-unit level. For each beach, RMSE and MAE were calculated using only the newly predicted pixels within the intertidal/foreshore zone (elevation range: -2 m to 10 m). These predictions were validated against the airborne Lidar DEM. Fig. 11 illustrates the distribution of these error metrics, distinguishing between beaches that contained ICESat-2 training samples and those that did not.

As shown in the statistical summary, sites with ICESat-2 samples (n = 148) achieved mean RMSE = 0.93 m and MAE = 0.74 m. In comparison, beaches without samples (n = 223) had slightly higher errors (mean RMSE = 1.02 m, MAE = 0.85 m). Violin plots (Fig. 11a, b) further show that the group with training data has a tighter error distribution with fewer outliers, whereas the untrained group shows broader variability. Although local training data yields a measurable improvement in accuracy and stability, the performance gap is narrow. This demonstrates the model's robust cross-beach transferability, allowing effective reconstruction of intertidal gaps even where direct ICESat-2 data are absent.

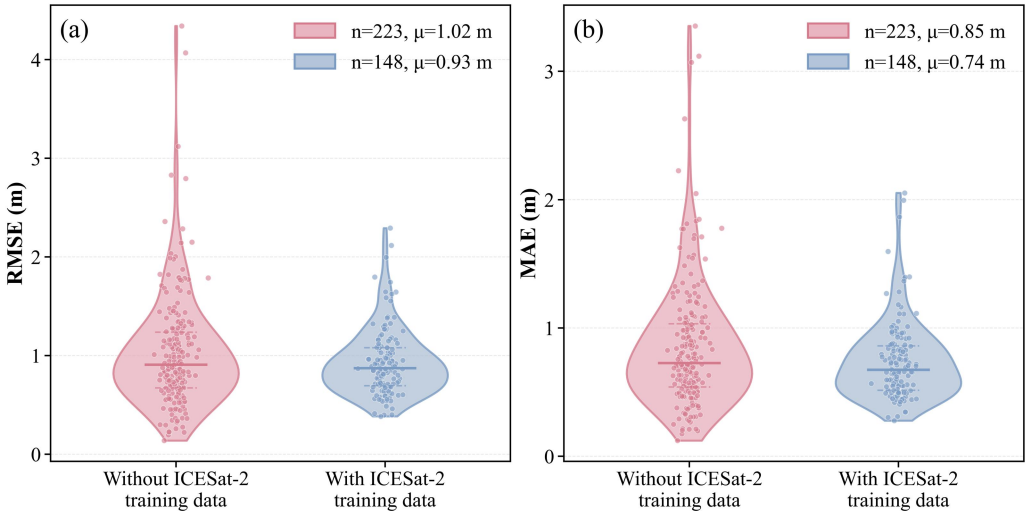

Fig. 11. Assessment of model transferability based on the accuracy of reconstructed intertidal topography. Comparison of per-beach error metrics between beaches with and without ICESat-2 training data. (a) RMSE and (b) MAE distributions computed exclusively for the gap-filled intertidal pixels against the airborne Lidar DEM. The legends indicate the number of beaches (n) and the group mean error (μ).

4.5 Interpretation of feature importance using SHAP analysis

Based on the computed SHAP values, three types of visualizations were generated to interpret the model from different perspectives. The first is the SHAP summary plot, which simultaneously conveys feature importance and the direction of impact. Features are ranked in descending order of global significance, represented by their mean absolute SHAP values. Each

https://doi.org/10.5194/essd-2025-826
Preprint. Discussion started: 30 January 2026

point in the plot corresponds to a single sample; the color indicates the magnitude of the feature value, while the horizontal position denotes the direction (positive or negative) and strength of its contribution to the prediction. This visualization provides a global overview of the model's decision-making process. The second visualization is the SHAP feature-interaction heatmap, which illustrates the average interaction intensity between pairs of important features. This representation highlights synergistic relationships and helps elucidate the complex interactions that influence the model's predictive behavior. Finally, the SHAP dependence plot was used to investigate the effects of individual features further. For the six most important features identified in the summary plot, dependence graphs were generated to show the relationship between each feature's actual value and its corresponding SHAP value. These plots clearly reveal the nonlinear dependencies between single features and the model's predicted output.

High near-infrared (NIR) reflectance is strongly associated with higher predicted beach elevation (Fig. 12(a)). Among all predictors, B8_20p (the 20th percentile of the near-infrared band) contributes most positively to the model output. This indicates that the model effectively leverages the physical principle of strong water absorption in the NIR spectrum to distinguish terrain. High NIR values correspond to dry, exposed supratidal sands, whereas low NIR values are characteristic of frequently inundated intertidal zones where moisture and water coverage significantly attenuate the signal. Conversely, B3_20p (the 20th percentile of the green band) has the strongest negative effect. High green-band reflectance is typically associated with shallow water bodies or moist sediments in low-lying areas, which the model correctly interprets as indicators of lower elevation. Geometric and positional features such as In_dis, Coast_dis, Co_ratio, X, and Y also rank among the most influential variables. This indicates the model uses spatial context to enforce a realistic topographic structure, ensuring predicted elevations follow a plausible cross-shore geomorphological gradient.

The distribution of SHAP values across all samples confirms the dominant mechanisms driving the intertidal reconstruction (Fig. 12(b)). B8_20p shows a clear positive contribution trend, while B3_20p exhibits variable and opposing effects. This implies that the model relies heavily on the moisture-sensitive NIR band to resolve the primary elevation gradient from the sea to the land. Spatial and geometric features consistently show positive SHAP values, reinforcing their supportive role in refining the spatial continuity of the beach profile. The variability in SHAP values arises from the heterogeneity of coastal conditions, demonstrating that the model captures distinct spectral-topographic relationships across the backshore, foreshore, and intertidal zones.

Nonlinear feature responses further clarify how the model resolves the intertidal interface (Fig. 12(c)). B8_20p exhibits a sharp monotonic increase in SHAP values at lower reflectance ranges before stabilizing at high levels. This steep rising segment precisely corresponds to the transition from the wet intertidal zone to the dry backshore, demonstrating that the model is highly sensitive to moisture changes in this critical gap region. In contrast, B3_20p displays a pronounced negative trend that levels off at moderate reflectance, confirming its association with low-lying wet areas or shallow water. In_dis shows a nonlinear response with substantial variability, reflecting the complex morphological transition between landward and seaward beach zones. B8_50p follows a positive trend similar to B8_20p but with earlier saturation. This difference suggests that using multi-percentile statistics allows the model to capture temporal variations in tidal exposure, which is essential for determining

https://doi.org/10.5194/essd-2025-826
Preprint. Discussion started: 30 January 2026

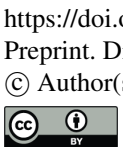

Open Access Earth System Science Data Discussions

elevation in dynamically wetted areas. Geographic coordinates (X, Y) reveal broad spatial gradients in predicted elevation that are further modulated by spectral variables, indicating regional-scale variations in coastal morphology captured by the model.

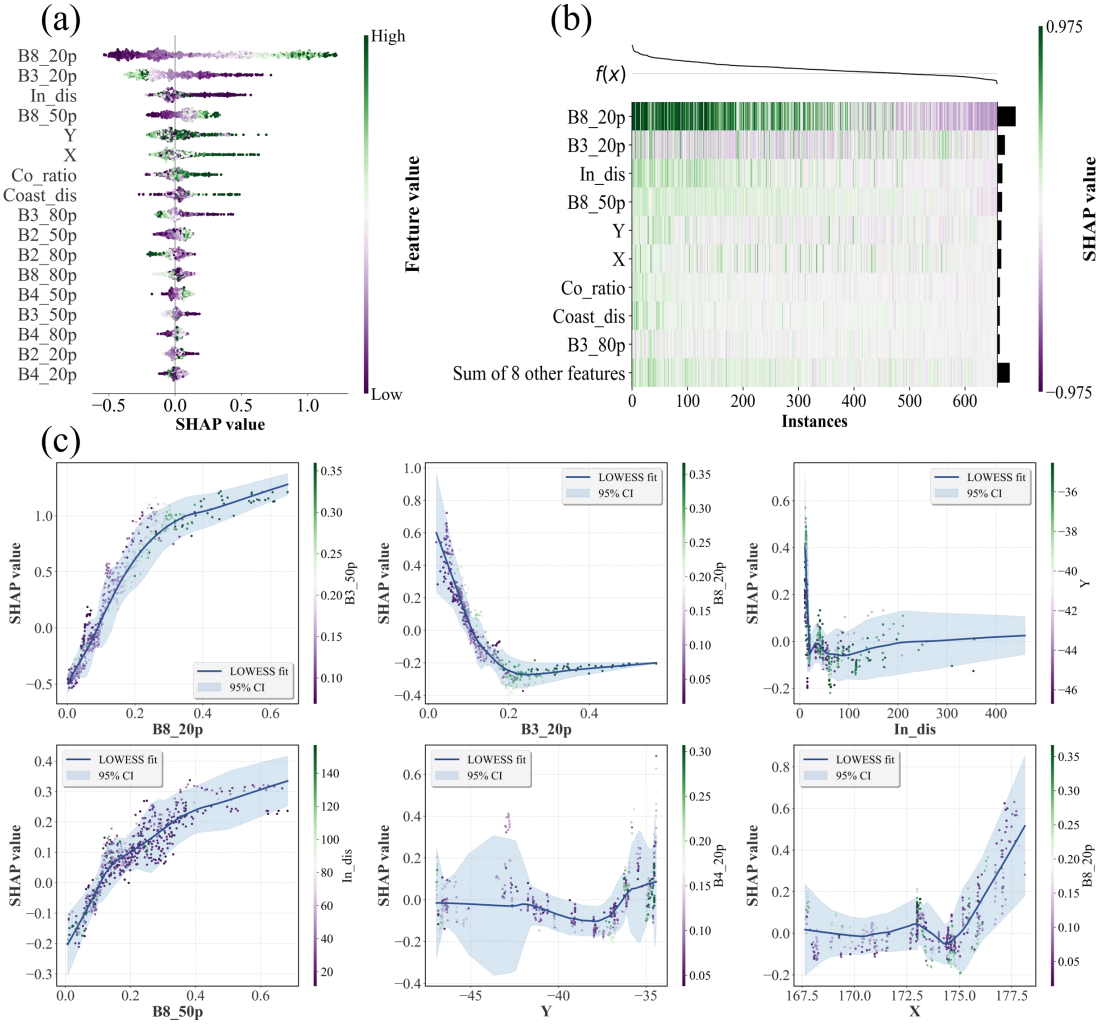

Fig. 12. SHAP-based model interpretation visualizations. (a) Summary plot depicting the importance and direction of effect for the 17 input features on elevation predictions, with a purple-to-green (PRGn) color gradient (purple = low feature values, white = intermediate, green = high). The horizontal axis indicates the SHAP value, and the vertical axis lists the feature names. (b) Heatmap, ordered by samples, displaying features and their corresponding SHAP contributions (PRGn color scale). The right-side bar plots indicate global feature importance. (c) Dependence plots for the top six most important features, where the PRGn color gradient reflects the value of the interacting feature, and the blue line/shaded band show the LOWESS fit and its 95% confidence interval.

https://doi.org/10.5194/essd-2025-826
Preprint. Discussion started: 30 January 2026

5 Discussion

5.1. Rationality of selecting DeltaDTM

To validate the selection of DeltaDTM as the backshore baseline, we comprehensively evaluated available global elevation products. We excluded coarse-resolution datasets such as GLL_DTM_v2, CoastalDEM, and MERIT DEM (~90 m), as their resolution is too low to capture beach micro-topography (Kulp and Strauss, 2018; Vernimmen and Hooijer, 2023; Yamazaki et al., 2017). Consequently, we focused on seven high-resolution (~30 m) global products: DeltaDTM, DiluviumDEM, AW3D30, Copernicus DEM, FABDEM, NASADEM, and SRTM (Esa, 2024; Hawker et al., 2022; Nasa, 2020). The assessment was rigorously conducted at both beach-unit and aggregated scales, with airborne Lidar serving as the validation benchmark. Analyses were strictly limited to the elevation range of -2 m to 10 m.

Fig. 13(a)-(b) show boxplots of per-beach spatial coverage and vertical accuracy (RMSE), illustrating site-to-site variability. Similarly, Fig. 13c, d provide aggregated statistics for the entire study area, giving a holistic performance overview. The results reveal a critical trade-off between coverage and accuracy. In coverage (Fig. 13a,c), conventional, gap-filled DEMs have a clear advantage: NASADEM achieves the highest coverage (58.7%), followed by SRTMDEM (56.0%) and AW3DDSM (53.8%). Among coastal-corrected products, DiluviumDEM, FABDEM, and COP30DEM show similar coverage (about 47%). Notably, DeltaDTM has the lowest overall coverage (46.9%), reflecting its strict quality control that excludes uncertain intertidal pixels.

However, the accuracy assessment (Fig. 13b,d) shows that DeltaDTM’ s conservative masking yields the highest vertical reliability. Due to vegetation bias and lack of tidal corrections, general-purpose datasets (SRTMDEM, NASADEM, AW3DDSM) perform poorly, with RMSEs exceeding 2.7 m (Fig. 13d). Among the better-performing candidates, DeltaDTM achieves the highest overall accuracy (RMSE = 1.37 m). COP30DEM (1.39 m) and FABDEM (1.49 m) are close competitors but slightly less accurate. Despite its coastal design, DiluviumDEM shows a higher RMSE (1.66 m), suggesting its interpolation strategy introduces vertical uncertainty.In summary, although DeltaDTM provides the least spatial coverage, it achieves the highest vertical accuracy among all evaluated 30-m products. For our framework, minimizing baseline vertical error is prioritized over initial coverage, as systematic biases are difficult to correct. Therefore, DeltaDTM was selected as the optimal vertical reference, providing the most accurate structural foundation. The NZ-BeachTopo30 dataset supplements this foundation with the missing intertidal zones. It yields a complete dataset that outperforms all individual existing products.

https://doi.org/10.5194/essd-2025-826
Preprint. Discussion started: 30 January 2026

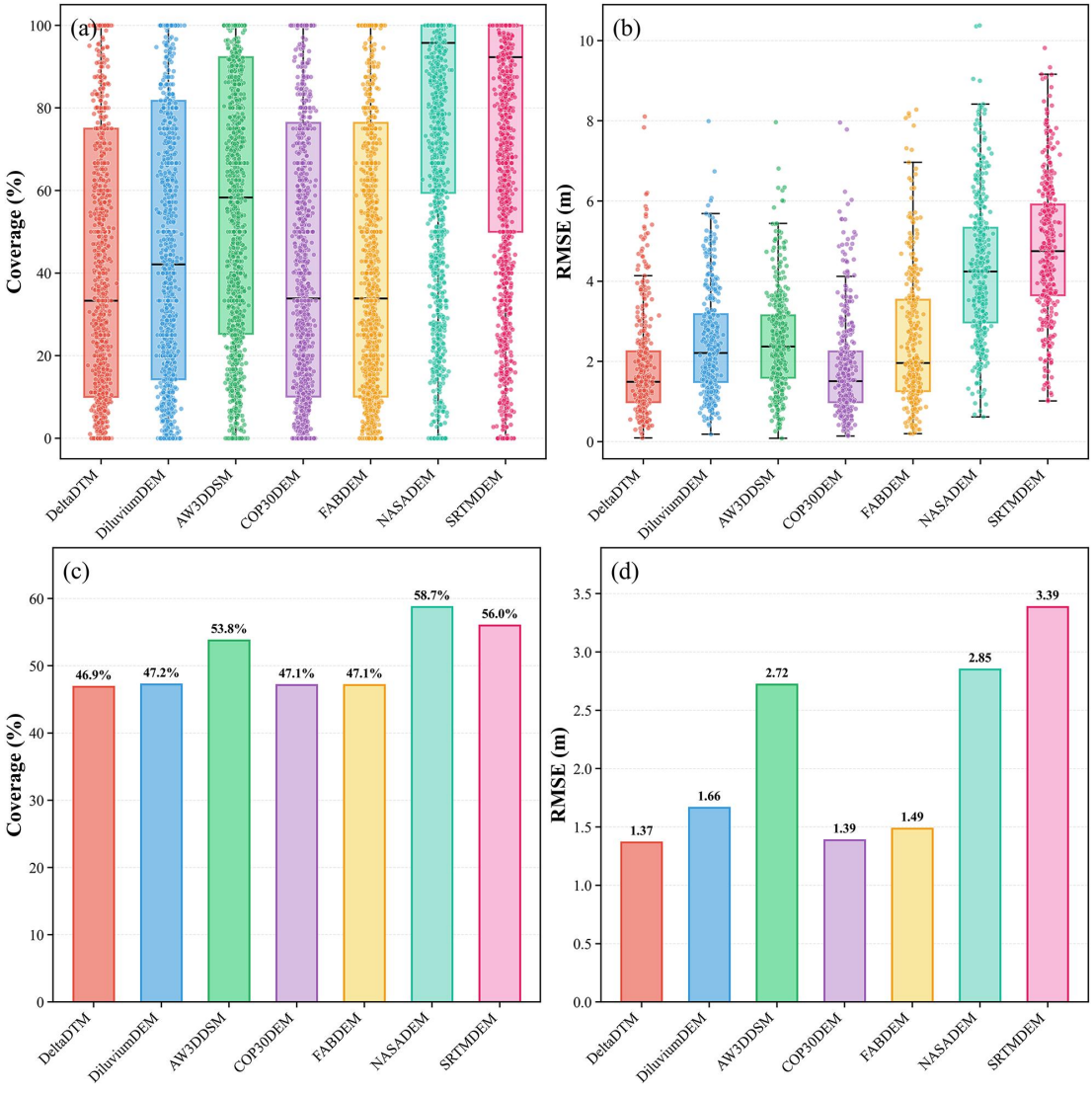

Fig. 13. Comparison of spatial coverage and vertical accuracy among seven global topographic datasets. (a) Boxplot comparison of the spatial coverage (percentage of valid pixels) per beach unit. (b) Boxplot comparison of vertical accuracy (RMSE) per beach unit assessed against airborne Lidar DEM data. (c) Aggregated spatial coverage percentages for the entire study area. (d) Aggregated vertical accuracy (RMSE) calculated for the entire study area. The datasets evaluated include DeltaDTM, DiluviumDEM, AW3DDSM, COP30DEM, FABDEM, NASADEM, and SRTMDEM.

5.2. Implications for sea-level rise inundation assessment

As global warming intensifies, sea-level rise has become one of the most prominent climate change-induced threats to coastal ecosystems and human settlements. The Intergovernmental Panel on Climate Change (IPCC) has predicted that global sea level will rise by 40 to 90 centimeters by the end of the 21st century, and regional variations may lead to even higher local sea-level rises in some coastal areas (Ipcc, 2023). Such changes will significantly increase the risk of coastal inundation, especially

https://doi.org/10.5194/essd-2025-826
Preprint. Discussion started: 30 January 2026

for low-elevation zones like beaches, intertidal zones and foreshores. Accurate assessment of inundation extent under sea level rise scenarios is therefore crucial for formulating scientific coastal management strategies and disaster prevention measures.

To address this need and verify the reliability of topographic datasets in inundation assessment, this study conducted a focused analysis. Using the airborne Lidar DEM as the ground truth, 335 beaches with complete Lidar coverage were selected within the study area. The inundation area under a 1 m sea-level rise scenario was calculated for three datasets including DeltaDTM, NZ-BeachTopo30, and the Lidar DEM. To simulate realistic inundation, a hydrological connectivity analysis was applied using a 4-connected neighborhood rule. First, based on the preprocessed coastline (Section 3.1.3), pixels with elevation $\leqslant$ 1 m were identified as initially inundable. Then, using a 4-connected rule (considering only edge-adjacent pixels), the algorithm iteratively expanded this area by adding any connected pixel also $\leqslant$ 1 m, continuing until no new pixels qualified. Finally, the inundation area was calculated by summing the areas of all inundated pixels. All datasets were projected into NZTM2000 to ensure spatial accuracy during area calculation. Based on the Lidar-derived inundation results, the inundation areas from DeltaDTM and NZ-BeachTopo30 were plotted against their corresponding Lidar values as scatter plots (Fig. 14a, b), enabling a quantitative assessment of their accuracy under sea-level-rise scenarios. Additionally, to visually compare inundation extents, spatial pattern maps were generated for two randomly selected beach units (Fig. 14c, d), highlighting the differences between DeltaDTM and NZ-BeachTopo30. Fig. 14(a) (Lidar DEM vs. DeltaDTM) shows that the original DeltaDTM has obvious shortcomings in reflecting inundation area. Although the horizontal axis representing Lidar inundation area has a wide variation range, the vertical axis representing the corresponding inundation area from DeltaDTM is close to 0, resulting in a negative coefficient of determination (R^2 = -0.092). This indicates an extremely poor linear relationship between the DeltaDTM and Lidar DEM. Statistical error metrics also show large absolute deviations, with RMSE = 0.0378 km², MAE = 0.0111 km², and a negative mean bias error (MBE = -0.0108 km²). This suggests that DeltaDTM generally underestimates inundation area, as many points cluster near zero on the vertical axis, reflecting its lack of coverage in low-elevation intertidal zones. Technically, this underestimation is due to data gaps in DeltaDTM for intertidal zones and shoals, as well as limitations in resolution and acquisition timing. These factors prevent it from capturing actual inundable areas under low-elevation thresholds (e.g., 1 m), leading to severe underestimation of exposure under sea-level rise. In contrast, Fig. 14b (Lidar DEM vs. Predicted DEM) shows that NZ-BeachTopo30 agrees well with Lidar for inundation area estimation, with R^2 = 0.894 (indicating strong agreement), RMSE = 0.0118 km², MAE = 0.0048 km², and MBE = -0.0032 km². This high correlation is largely attributable to the accurate reconstruction of low-lying pixels ($\leqslant$ 1 m). As shown in Fig. 14a, the original DeltaDTM completely failed to capture these zones. Therefore, the reliable assessment of these high-risk areas is made possible solely by our gap-filling predictions. Fig. 14(c) and (d) illustrate the spatial inundation patterns of two representative beach units under a 1 m sea-level rise scenario. Both subplots clearly show that the result adds numerous relatively continuous inundation zones along the shoreline and within the intertidal low-lying areas. These newly added inundation areas are adjacent to the zones identified by DeltaDTM, effectively bridging gaps in the original coverage and extending inundation mapping into previously unrepresented intertidal zones. This pattern confirms that NZ-BeachTopo30 successfully supplements near-shore lowland

https://doi.org/10.5194/essd-2025-826
Preprint. Discussion started: 30 January 2026

topography, compensating for DeltaDTM's gaps by greatly improving the mapping of terrain ⩽ 1 m. This finding is fully consistent with the earlier statistical analysis. Consequently, these observations lead to two primary conclusions and several recommendations. First, from the perspective of emergency and risk assessment, the direct use of the original DeltaDTM under sea-level rise scenarios will significantly underestimate the inundated area, especially in low-elevation, sensitive zones such as intertidal zones and foreshores. Given that other open-source global or regional DEMs typically suffer from similar limitations in intertidal coverage and vertical accuracy, this issue of underestimation is likely prevalent in assessments relying on these datasets as well. Second, the XGBoost-based topographic reconstruction method proposed in this study, which integrates ICESat-2 and Sentinel-2 data, demonstrates high reliability in national-scale beach inundation assessment. It can significantly improve the accuracy of inundation area estimation, thereby providing more reliable data support for coastal management, risk assessment, and adaptation strategies such as flood zoning and ecological protection planning. It is important to highlight the following limitations: Inundation simulation relies on vertical datum and tidal level assumptions. This study uses a uniform 1 m increment relative to the EGM2008 datum, where 0 m is treated as Mean Sea Level (MSL), and does not account for local tidal levels, storm-surge superposition, or real-time tidal changes. Actual MSL often deviates from this idealized 0 m benchmark due to regional oceanographic and geodetic factors. Thus, the 1-m scenario primarily highlights the performance gap between products, rather than predicting absolute inundation. For more accurate sea-level rise inundation or erosion analysis, it is necessary to determine the precise local MSL height first and then conduct inundation simulations based on that. Additionally, for complex geomorphic areas such as extreme estuaries, tidal channels, or heavily engineered coastal segments, the model may still produce large case-specific errors. Therefore, in such areas, we recommend using high-resolution Lidar or field surveys for validation and correction, and integrating local MSL data for realistic assessments.

https://doi.org/10.5194/essd-2025-826
Preprint. Discussion started: 30 January 2026

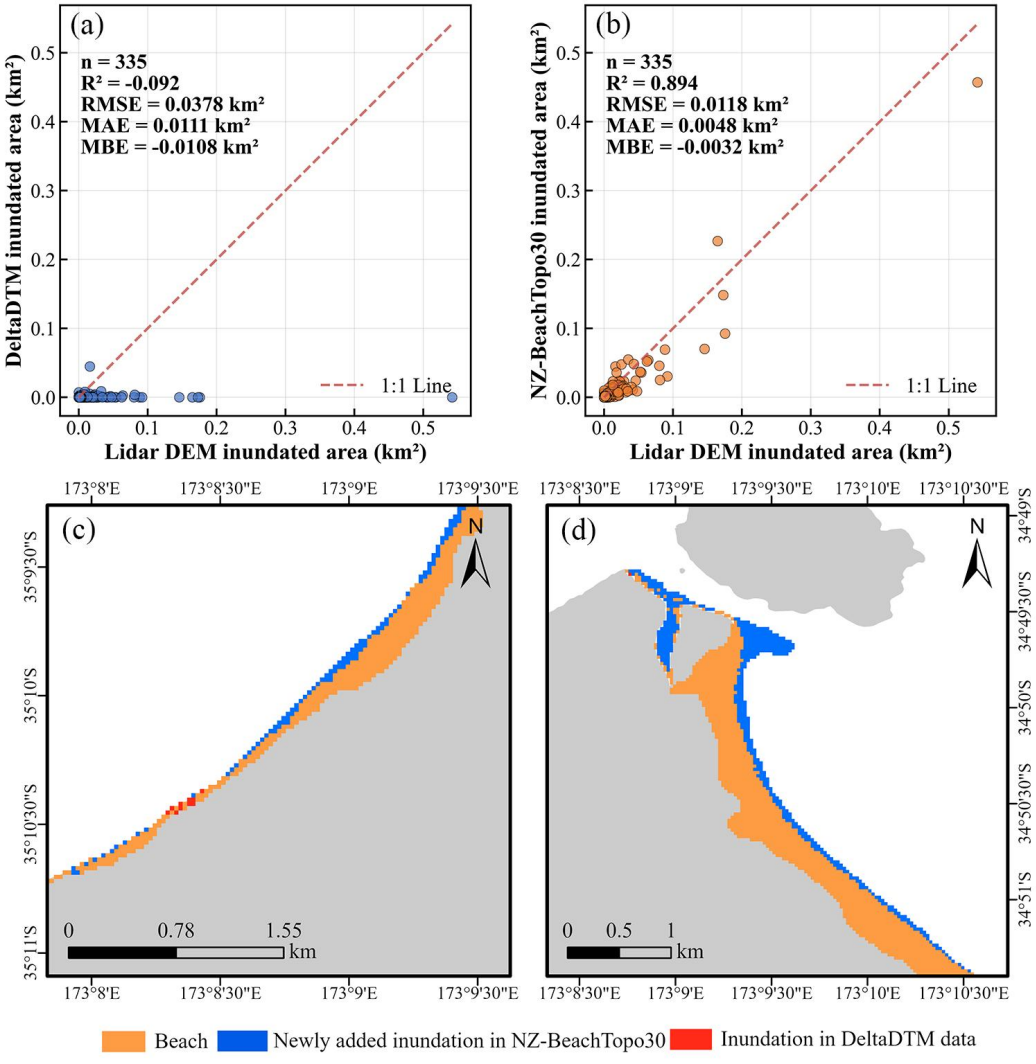

Fig. 14. Comparison of estimated inundation area and spatial patterns under a 1 m sea-level rise scenario. (a) Scatter plot of inundation area derived from the baseline DeltaDTM versus the Lidar DEM reference. (b) Scatter plot of inundation area derived from the NZ-BeachTopo30 dataset versus the Lidar DEM reference. (c) and (d) Spatial inundation patterns for two representative beach units. Orange areas indicate the beach extent, red areas indicate inundation simulated by the original DeltaDTM (inundation in DeltaDTM data), and blue areas indicate additional inundation identified by NZ-BeachTopo30 (newly added inundation in NZ-BeachTopo30). The land masks used as the background in panels (c) and (d) are from OSM.

5.3 Potential for global application and challenges

The method proposed in this study has strong potential for global application and scalability: the three core datasets used (ICESat-2, Sentinel-2, and DeltaDTM) are globally available, ensuring data accessibility for replication in other coastal regions. Specifically, for filling intertidal and shallow-water gaps in existing public DTMs (e.g., DeltaDTM), this method can directly enhance spatial coverage and topographic representativeness, thus offering broad applicability and practical utility.

https://doi.org/10.5194/essd-2025-826
Preprint. Discussion started: 30 January 2026

However, the robust global application of this method faces several challenges. First, regional variations in tidal regimes can alter the spectral-elevation relationship, affecting intertidal height retrieval. Second, the global heterogeneity in sediment properties, algal cover, and water reflectance means spectral features may not have universal topographic interpretations, complicating model transfer. Third, the non-uniform observation density and geometric distribution of ICESat-2 may leave some coastal segments with insufficient vertical control points. Fourth, the uneven global availability of high-precision validation data (e.g., airborne Lidar) hinders rigorous product assessment and error correction. Finally, in dynamic, complex environments like estuaries and engineered coasts, statistical models relying on spectra and sparse elevation points may struggle to capture intricate topographic details.5.4 Future considerations

The beach topography produced in this study has substantial application potential, with one of the most significant advantages being the ability to derive reliable beach slope metrics across the entire coastal profile. Because the reconstructed elevation surface is continuous from the backshore through the intertidal zone, slope can be calculated directly from the gridded product without requiring synchronous tidal information or instantaneous water-line observations (Vos et al., 2020). This continuity avoids the discontinuities, tidal artefacts, and segmentation errors that occur when slopes are estimated from traditional datasets that lack intertidal coverage, such as DeltaDTM or single-date shoreline-based methods. As a result, the derived cross-shore and alongshore slopes more accurately represent true morphology and are suitable for sediment budget analyses, erosion susceptibility assessment, coastal hazard classification, and parametrization of morphodynamic or wave-runup models. In addition to slope estimation, the continuous elevation data also improve the computation of profile curvature, beach volume, shoreline position metrics, and baseline topography for change detection. The inclusion of newly filled low-elevation areas strengthens the reliability of inundation and flood-risk modeling by reducing systematic underestimation of low-lying terrain. Furthermore, the dataset provides a consistent and vertically harmonized terrain reference that can be integrated into coastal planning, environmental management, emergency response, and calibration of local high-resolution surveys, offering a more robust foundation for national-scale coastal analyses.

To increase temporal fidelity, spatial resolution, and operational readiness, several technical developments should be pursued. First, static ancillary layers derived from OSM should be replaced or supplemented by time-resolved land cover and shoreline products based on Sentinel-2 time series, for example Google's Dynamic World and other Sentinel-2 LULC maps, which enable the definition of temporally varying beach extents and improve discrimination between transient tidal inundation and persistent surface types (Brown et al., 2022). Second, improving spatial granularity is achievable by leveraging the native 10 m Sentinel-2 bands together with denser sampling strategies for ICESat-2 control points or multiyear retracking approaches; this could support seasonal or annual 10 m reconstructions provided that co-registration, along-track footprint geometry, and sample density are carefully addressed and that targeted UAV or airborne Lidar surveys are used for local calibration and validation. Third, advanced modeling architectures and uncertainty aware frameworks merit exploration, because convolutional and attention based deep networks, graph neural networks, and physics informed models can better exploit spatial context and incorporate physical constraints, while ensemble, Bayesian, or Monte Carlo approaches can quantify predictive uncertainty to support probabilistic risk assessments. Fourth, feature engineering should be extended beyond single

https://doi.org/10.5194/essd-2025-826
Preprint. Discussion started: 30 January 2026

percentile predictors; multi percentile statistics such as p20, p50, and p80 of NDWI and NDVI, and percentile difference metrics such as NDWI p80 minus p20, encode exposure and tidal occurrence and can substantially improve prediction of intertidal elevation, and temporal trend indicators, texture measures, and SAR derived wetness or backscatter provide complementary information in cloudy or turbid conditions and should be evaluated systematically. Integrating these advancements will be key to achieving high-frequency, global-scale coastal monitoring with enhanced precision and operational readiness.

6. Data availability

The datasets in this study are available on Zenodo via the digital object identifier (DOI): https://doi.org/10.5281/zenodo.17785546 (Wang, 2025).

7. Conclusion

To bridge the persistent data gap within the dynamic intertidal zone, this study produced NZ-BeachTopo30. It stands as the first national-scale dataset to achieve full topographic coverage across the land-sea interface by fusing ICESat-2 altimetry and Sentinel-2 imagery. Distinct from conventional global DEMs that contain systematic voids due to tidal inundation, this dataset provides a seamless continuum from the stable backshore to the active foreshore. It specifically eliminates the disconnection between land and sea data. Through a nationwide case study in New Zealand, we demonstrate that the proposed framework can successfully reconstruct missing topography in intertidal and foreshore zones by employing an XGBoost model optimized with SMOGN-balanced samples.

The capability of the product to fill critical gaps is quantified by a significant 145.8% expansion in valid topographic coverage from 79.9 km² to 196.5 km². Meanwhile, it maintains strong overall agreement with airborne Lidar validation where R^2 is 0.75 and RMSE is 1.17 m. Our analysis confirmed that although DeltaDTM serves as an excellent stable baseline for backshore areas, it is severely limited by extensive coverage gaps in the intertidal zone. The proposed framework effectively addresses this limitation by seamlessly integrating predicted intertidal elevations with the DeltaDTM baseline, thereby providing sub-meter accuracy in these previously unmapped regions. Crucially, the recovered intertidal topography enabled reliable sea-level rise inundation modeling (R^2 = 0.894), effectively correcting the severe underestimation inherent in the original data-void baseline. Given the global availability of ICESat-2 and Sentinel-2 data, this framework offers a scalable solution to close the intertidal data gap worldwide, providing a continuous and robust foundation for coastal climate adaptation planning.

https://doi.org/10.5194/essd-2025-826
Preprint. Discussion started: 30 January 2026

Author contributions

The study was conceptualized by NX. YW, HX, WL, XL and CH collected the remote sensing and validation data and conducted the data per-processing. YW processed and analyzed the data, created figures and tables. EP, HX, JF, ZZ, YM and QL interpreted and discussed the results. YW, HX, CC, YC, YO and XG wrote the original draft and refined the figures. NX and QL contributed to project administration, funding acquisition and supervision. All the authors reviewed, discussed, revised and approved the final draft.

Competing interests

The authors declare that they have no conflict of interest.

Disclaimer

Acknowledgements

Financial support

This work was funded by the Disciplines Breakthrough Project in Aerospace Information and Spatiotemporal Intelligence, MOE, China, the National Key Research and Development Program of China [2024YFF0617900], the National Natural Science Foundation of China [42571378, 42101343], the Key Laboratory of Land Satellite Remote Sensing Application, Ministry of Natural Resources of the People's Republic of China [KLSMNR-K202309], the Natural Science Foundation of Jiangsu Province [BK20240258, BK20230441], the Jiangsu Marine Science and Technology Innovation Project [JSZRHYKJ202302], the Scientific Foundation for Youth Scholars of Shenzhen University [868-000001033431], Open-end Funds of Ministry of Education Key Laboratory for Earth System Modeling (Tsinghua University), and the Shenzhen Key Laboratory Program [SYSPG20241211173845013].

References

Amani, M., Ghorbanian, A., Ahmadi, S. A., Kakooei, M., Moghimi, A., Mirmazloumi, S. M., Moghaddam, S. H. A., Mahdavi, S., Ghahremanloo, M., Parsian, S., Wu, Q., and Brisco, B.: Google Earth Engine Cloud Computing Platform for Remote Sensing Big Data Applications: A Comprehensive Review, IEEE J. Sel. Top. Appl. Earth Obs. Remote Sens., 13, 5326-5350, https://doi.org/10.1109/JSTARS.2020.3021052, 2020.

Baetens, L., Desjardins, C., and Hagolle, O.: Validation of Copernicus Sentinel-2 Cloud Masks Obtained from MAJA, Sen2Cor, and FMask Processors Using Reference Cloud Masks Generated with a Supervised Active Learning Procedure, Remote Sens., 11, https://doi.org/10.3390/rs11040433, 2019.

https://doi.org/10.5194/essd-2025-826
Preprint. Discussion started: 30 January 2026

785 Bishop-Taylor, R., Sagar, S., Lymburner, L., and Beaman, R. J.: Between the tides: Modelling the elevation of Australia's exposed intertidal zone at continental scale, Estuarine Coastal Shelf Sci., 223, 115-128, https://doi.org/10.1016/j.ecss.2019.03.006, 2019.

Branco, P., Torgo, L., and Ribeiro, R. P.: SMOGN: a Pre-processing Approach for Imbalanced Regression, in: Proceedings of Machine Learning Research, 36-50, 2017.

790 Brown, C. F., Brumby, S. P., Guzder-Williams, B., Birch, T., Hyde, S. B., Mazzariello, J., Czerwinski, W., Pasquarella, V. J., Haertel, R., Ilyushchenko, S., Schwehr, K., Weisse, M., Stolle, F., Hanson, C., Guinan, O., Moore, R., and Tait, A. M.: Dynamic World, Near real-time global 10 m land use land cover mapping, Sci. Data, 9, 251, https://doi.org/10.1038/s41597-022-01307-4, 2022.

Burvingt, O., Castelle, B., Marieu, V., Lubac, B., Nicolae Lerma, A., and Robin, N.: Using Pleiades Satellite Imagery to
795 Monitor Multi-Annual Coastal Dune Morphological Changes, Remote Sens., 17, https://doi.org/10.3390/rs17091522, 2025.

Caffyn, A., Prosser, B., and Jobbins, G.: A Framework for the analysis of socio-economic impacts on beach environments, Baseline research for the integrated sustainable management of Mediterranean sensitive coastal ecosystems, 37-50, 2002.

Casella, E., Drechsel, J., Winter, C., Benninghoff, M., and Rovere, A.: Accuracy of sand beach topography surveying by
800 drones and photogrammetry, Geo-Mar. Lett., 40, 255-268, https://doi.org/10.1007/s00367-020-00638-8, 2020.

Chawla, N., Bowyer, K., Hall, L., and Kegelmeyer, W.: SMOTE: Synthetic Minority Over-sampling Technique, ArXiv, https://doi.org/10.1613/jair.953, 2002.

Chen, C., Zhang, C., Tian, B., Wu, W., and Zhou, Y.: Tide2Topo: A new method for mapping intertidal topography accurately in complex estuaries and bays with time-series Sentinel-2 images, ISPRS J. Photogramm. Remote Sens., 200, 55-72,
805 https://doi.org/10.1016/j.isprsjprs.2023.05.004, 2023.

Chen, T. and Guestrin, C.: XGBoost: A Scalable Tree Boosting System, in: Proceedings of the 22nd ACM SIGKDD International Conference on Knowledge Discovery and Data Mining, San Francisco, CA, USA, 785–794, 2016.

Defeo, O., McLachlan, A., Armitage, D., Elliott, M., and Pittman, J.: Sandy beach social–ecological systems at risk: regime shifts, collapses, and governance challenges, Front. Ecol. Environ., 19, 564-573, https://doi.org/10.1002/fee.2406, 2021.

810 Dusseau, D., Zobel, Z., and Schwalm, C. R.: DiluviumDEM: Enhanced accuracy in global coastal digital elevation models, Remote Sens. Environ., 298, 113812, https://doi.org/10.1016/j.rse.2023.113812, 2023.

ESA: Copernicus Global Digital Elevation Model, European Space Agency [data set], https://doi.org/10.5270/ESA-c5d3d65, 2024.

Farr, T. G., Rosen, P. A., Caro, E., Crippen, R., Duren, R., Hensley, S., Kobrick, M., Paller, M., Rodriguez, E., Roth, L., Seal,
815 D., Shaffer, S., Shimada, J., Umland, J., Werner, M., Oskin, M., Burbank, D., and Alsdorf, D.: The Shuttle Radar Topography Mission, Rev. Geophys., 45, https://doi.org/10.1029/2005RG000183, 2007.

https://doi.org/10.5194/essd-2025-826
Preprint. Discussion started: 30 January 2026

Graffin, M., Touzé, T., Bergsma, E. W. J., and Almar, R.: Towards a global assessment of sandy shorelines: Systematic extraction and validation of optical satellite-derived coastal indicators at various sites, Remote Sens. Environ., 331, 115033, https://doi.org/10.1016/j.rse.2025.115033, 2025.

Hamling, I. J., Wright, T. J., Hreinsdóttir, S., and Wallace, L. M.: A Snapshot of New Zealand's Dynamic Deformation Field From Envisat InSAR and GNSS Observations Between 2003 and 2011, Geophys. Res. Lett., 49, e2021GL096465, https://doi.org/10.1029/2021GL096465, 2022.

Hanley, M. E., Hoggart, S. P. G., Simmonds, D. J., Bichot, A., Colangelo, M. A., Bozzeda, F., Heurtefeux, H., Ondiviela, B., Ostrowski, R., Recio, M., Trude, R., Zawadzka-Kahlau, E., and Thompson, R. C.: Shifting sands? Coastal protection by sand banks, beaches and dunes, Coastal Eng., 87, 136-146, https://doi.org/10.1016/j.coastaleng.2013.10.020, 2014.

Hawker, L., Uhe, P., Paulo, L., Sosa, J., Savage, J., Sampson, C., and Neal, J.: A 30 m global map of elevation with forests and buildings removed, Environ. Res. Lett., 17, 024016, https://doi.org/10.1088/1748-9326/ac4d4f, 2022.

He, H. and Garcia, E. A.: Learning from Imbalanced Data, IEEE Trans. Knowl. Data Eng., 21, 1263-1284, https://doi.org/10.1109/TKDE.2008.239, 2009.

IPCC: Ocean, Cryosphere and Sea Level Change, Climate Change 2021 – The Physical Science Basis: Working Group I Contribution to the Sixth Assessment Report of the Intergovernmental Panel on Climate Change, Cambridge University Press, Cambridge, 1211-1362 pp., ISBN 9781009157889, 2023.

Jacoby, W. G.: Loess:: a nonparametric, graphical tool for depicting relationships between variables, Electoral Studies, 19, 577-613, https://doi.org/10.1016/S0261-3794(99)00028-1, 2000.

Kroon, A., Davidson, M. A., Aarninkhof, S. G. J., Archetti, R., Armaroli, C., Gonzalez, M., Medri, S., Osorio, A., Aagaard, T., Holman, R. A., and Spanhoff, R.: Application of remote sensing video systems to coastline management problems, Coastal Eng., 54, 493-505, https://doi.org/10.1016/j.coastaleng.2007.01.004, 2007.

Kulp, S. A. and Strauss, B. H.: CoastalDEM: A global coastal digital elevation model improved from SRTM using a neural network, Remote Sens. Environ., 206, 231-239, https://doi.org/10.1016/j.rse.2017.12.026, 2018.

Lao, J., Wang, C., Zhu, X., Xi, X., Nie, S., Wang, J., Cheng, F., and Zhou, G.: Retrieving building height in urban areas using ICESat-2 photon-counting LiDAR data, Int. J. Appl. Earth Obs. Geoinf., 104, 102596, https://doi.org/10.1016/j.jag.2021.102596, 2021.

Li, M., Chen, B., Webster, C., Gong, P., and Xu, B.: The land-sea interface mapping: China's coastal land covers at 10 m for 2020, Sci. Bull., 67, 1750-1754, https://doi.org/10.1016/j.scib.2022.07.012, 2022.

Luijendijk, A., Hagenaars, G., Ranasinghe, R., Baart, F., Donchyts, G., and Aarninkhof, S.: The State of the World's Beaches, Sci. Rep., 8, 6641, https://doi.org/10.1038/s41598-018-24630-6, 2018.

Lundberg, S., Erion, G., Chen, H., DeGrave, A., Prutkin, J., Nair, B., Katz, R., Himmelfarb, J., Bansal, N., and Lee, S.-I.: From local explanations to global understanding with explainable AI for trees, Nat. Mach. Intell., 2, 56-67, https://doi.org/10.1038/s42256-019-0138-9, 2020.

https://doi.org/10.5194/essd-2025-826
Preprint. Discussion started: 30 January 2026

Lundberg, S. M.: A Unified Approach to Interpreting Model Predictions, arXiv [preprint], https://doi.org/10.48550/arXiv.1705.07874, 2017.

Ma, Y., Wang, L., Xu, N., Zhang, S., Hua Wang, X., and Li, S.: Estimating coastal slope of sandy beach from ICESat-2: a case study in Texas, Environ. Res. Lett., 18, 044039, https://doi.org/10.1088/1748-9326/acc87d, 2023.

Mao, Y., Harris, D. L., Xie, Z., and Phinn, S.: Efficient measurement of large-scale decadal shoreline change with increased accuracy in tide-dominated coastal environments with Google Earth Engine, ISPRS J. Photogramm. Remote Sens., 181, 385-399, https://doi.org/10.1016/j.isprsjprs.2021.09.021, 2021.

Markus, T., Neumann, T., Martino, A., Abdalati, W., Brunt, K., Csatho, B., Farrell, S., Fricker, H., Gardner, A., Harding, D., Jasinski, M., Kwok, R., Magruder, L., Lubin, D., Luthcke, S., Morison, J., Nelson, R., Neuenschwander, A., Palm, S., Popescu, S., Shum, C. K., Schutz, B. E., Smith, B., Yang, Y., and Zwally, J.: The Ice, Cloud, and land Elevation Satellite-2 (ICESat-2): Science requirements, concept, and implementation, Remote Sens. Environ., 190, 260-273, https://doi.org/10.1016/j.rse.2016.12.029, 2017.

Meng, J., Xu, D., Tao, Z., and Ge, Q.: Sandy Beach Extraction Method Based on Multi-Source Data and Feature Optimization: A Case in Fujian Province, China, Remote Sens., 17, https://doi.org/10.3390/rs17162754, 2025.

NASA, J.: NASADEM Merged DEM Global 1 arc second V001, NASA Land Processes Distributed Active Archive Center [data set], https://doi.org/10.5067/MEASURES/NASADEM/NASADEM_HGT.001, 2020.

Nel, R., Campbell, E. E., Harris, L., Hauser, L., Schoeman, D. S., McLachlan, A., du Preez, D. R., Bezuidenhout, K., and Schlacher, T. A.: The status of sandy beach science: Past trends, progress, and possible futures, Estuarine Coastal Shelf Sci., 150, 1-10, https://doi.org/10.1016/j.ecss.2014.07.016, 2014.

Ni, M., Xu, N., Ou, Y., Yao, J., Li, Z., Mo, F., Huang, C., Xin, H., and Xu, H.: The first 10-m China's national-scale sandy beach map in 2022 derived from Sentinel-2 imagery, Int. J. Digital Earth, 17, 2425163, https://doi.org/10.1080/17538947.2024.2425163, 2024.

Prakash Mohanty, M., Nithya, S., Nair, A. S., Indu, J., Ghosh, S., Mohan Bhatt, C., Srinivasa Rao, G., and Karmakar, S.: Sensitivity of various topographic data in flood management: Implications on inundation mapping over large data-scarce regions, J. Hydrol., 590, 125523, https://doi.org/10.1016/j.jhydrol.2020.125523, 2020.

Pronk, M., Hooijer, A., Eilander, D., Haag, A., de Jong, T., Vousdoukas, M., Vernimmen, R., Ledoux, H., and Eleveld, M.: DeltaDTM: A global coastal digital terrain model, Sci. Data, 11, 273, https://doi.org/10.1038/s41597-024-03091-9, 2024.

Salameh, E., Desroches, D., Deloffre, J., Fjørtoft, R., Mendoza, E. T., Turki, I., Froideval, L., Levaillant, R., Déchamps, S., Picot, N., Laignel, B., and Frappart, F.: Evaluating SWOT's interferometric capabilities for mapping intertidal topography, Remote Sens. Environ., 314, 114401, https://doi.org/10.1016/j.rse.2024.114401, 2024.

Salameh, E., Frappart, F., Almar, R., Baptista, P., Heygster, G., Lubac, B., Raucoules, D., Almeida, L. P., Bergsma, E. W. J., Capo, S., De Michele, M., Idier, D., Li, Z., Marieu, V., Poupardin, A., Silva, P. A., Turki, I., and Laignel, B.: Monitoring Beach Topography and Nearshore Bathymetry Using Spaceborne Remote Sensing: A Review, Remote Sens., 11, https://doi.org/10.3390/rs11192212, 2019.

https://doi.org/10.5194/essd-2025-826
Preprint. Discussion started: 30 January 2026

Schmelz, W. J. and Psuty, N. P.: Application of geomorphological maps and LiDAR to volumetrically measure coastal geomorphological change from Hurricane Sandy at Fire Island National Seashore, Geomorphology, 408, 108262, https://doi.org/10.1016/j.geomorph.2022.108262, 2022.

Shwartz-Ziv, R. and Armon, A.: Tabular data: Deep learning is not all you need, Inf. Fusion, 81, 84-90, https://doi.org/10.1016/j.inffus.2021.11.011, 2022.

Snyder, J. P.: Map projections: A working manual, Washington, D.C., Report 1395, 1987.

Stockdon, H. F., Holman, R. A., Howd, P. A., and Sallenger, A. H.: Empirical parameterization of setup, swash, and runup, Coastal Eng., 53, 573-588, https://doi.org/10.1016/j.coastaleng.2005.12.005, 2006.

Takaku, J., Tadono, T., Tsutsui, K., and Ichikawa, M.: VALIDATION OF "AW3D" GLOBAL DSM GENERATED FROM ALOS PRISM, ISPRS Ann. Photogramm. Remote Sens. Spatial Inf. Sci., III-4, 25-31, https://doi.org/10.5194/isprs-annals-III-4-25-2016, 2016.

Turner, I. L., Harley, M. D., Short, A. D., Simmons, J. A., Bracs, M. A., Phillips, M. S., and Splinter, K. D.: A multi-decade dataset of monthly beach profile surveys and inshore wave forcing at Narrabeen, Australia, Sci. Data, 3, 160024, https://doi.org/10.1038/sdata.2016.24, 2016.

Vernimmen, R. and Hooijer, A.: New LiDAR-Based Elevation Model Shows Greatest Increase in Global Coastal Exposure to Flooding to Be Caused by Early-Stage Sea-Level Rise, Earth's Future, 11, e2022EF002880, https://doi.org/10.1029/2022EF002880, 2023.

Vitousek, S., Buscombe, D., Vos, K., Barnard, P. L., Ritchie, A. C., and Warrick, J. A.: The future of coastal monitoring through satellite remote sensing, Cambridge Prisms: Coastal Futures, 1, e10, https://doi.org/10.1017/cft.2022.4, 2023.

Vos, K., Harley, M. D., Splinter, K. D., Simmons, J. A., and Turner, I. L.: Sub-annual to multi-decadal shoreline variability from publicly available satellite imagery, Coastal Eng., 150, 160-174, https://doi.org/10.1016/j.coastaleng.2019.04.004, 2019.

Vos, K., Harley, M. D., Splinter, K. D., Walker, A., and Turner, I. L.: Beach Slopes From Satellite-Derived Shorelines, Geophys. Res. Lett., 47, e2020GL088365, https://doi.org/10.1029/2020GL088365, 2020.

Vousdoukas, M. I., Ranasinghe, R., Mentaschi, L., Plomaritis, T. A., Athanasiou, P., Luijendijk, A., and Feyen, L.: Sandy coastlines under threat of erosion, Nat. Clim. Change, 10, 260-263, https://doi.org/10.1038/s41558-020-0697-0, 2020.

Wang, Y.: New Zealand National-Scale Beach Topography Dataset (30 m): A Fusion of ICESat-2 and Sentinel-2, Zenodo [data set], https://doi.org/10.5281/zenodo.17785546, 2025.

Wang, Y. and Sherry Ni, X.: A XGBoost Risk Model via Feature Selection and Bayesian Hyper-Parameter Optimization, International Journal of Database Management Systems, 11, 1-17, https://doi.org/10.5121/ijdms.2019.11101, 2019.

Wang, Y., Huang, C., Ma, Y., Ma, X., Ou, Y., Chen, C., Li, B., Zhou, S., Jia, D., Wang, Z., Li, Q., and Xu, N.: Combining Airborne LiDAR Data and Optical Imagery for Improved National-Scale Beach Topography Estimation: A Case Study in New Zealand, IEEE Trans. Geosci. Remote Sens., 63, 1-23, https://doi.org/10.1109/TGRS.2025.3635047, 2025.

https://doi.org/10.5194/essd-2025-826
Preprint. Discussion started: 30 January 2026

Wen, Z., Wang, Q., Ma, Y., Jacinthe, P. A., Liu, G., Li, S., Shang, Y., Tao, H., Fang, C., Lyu, L., Zhang, B., and Song, K.: Remote estimates of suspended particulate matter in global lakes using machine learning models, Int. Soil Water Conserv. Res., 12, 200-216, https://doi.org/10.1016/j.iswcr.2023.07.002, 2024.

Xu, N. and Gong, P.: Significant coastline changes in China during 1991–2015 tracked by Landsat data, Sci. Bull., 63, 883-886, https://doi.org/10.1016/j.scib.2018.05.032, 2018.

Xu, N., Zhou, C., and Zhang, S.: Inferring coastal slope of sandy beaches from remote sensing imagery and tidal level data, Geocarto Int., 39, 2405141, https://doi.org/10.1080/10106049.2024.2405141, 2024a.

Xu, N., Wang, L., Ma, Y., Ma, X., and Wang, X. H.: Constructing intertidal topography for sandy beaches by combining Sentinel-2 imagery and water level data, Geo-spatial Inf. Sci., 1-15, https://doi.org/10.1080/10095020.2024.2449453, 2025.

Xu, N., Wang, L., Xu, H., Ma, Y., Li, Y., and Wang, X. H.: Deriving Accurate Intertidal Topography for Sandy Beaches Using ICESat-2 Data and Sentinel-2 Imagery, J. Remote Sens., 4, https://doi.org/10.34133/remotesensing.0305, 2024b.

Yamazaki, D., Ikeshima, D., Tawatari, R., Yamaguchi, T., O'Loughlin, F., Neal, J. C., Sampson, C. C., Kanae, S., and Bates, P. D.: A high-accuracy map of global terrain elevations, Geophys. Res. Lett., 44, 5844-5853, https://doi.org/10.1002/2017GL072874, 2017.

Yao, S., Tan, K., Wang, Y., Zhang, W., Liu, S., and Yang, J.: Estimating terrain elevations at 10 m resolution by Integrating random forest machine learning model and ICESat-2, Sentinel-1, and Sentinel-2 satellite remotely sensed data, Int. J. Appl. Earth Obs. Geoinf., 132, 104010, https://doi.org/10.1016/j.jag.2024.104010, 2024.

Yao, S., Zhu, J., Zhang, W., Tian, B., Sun, W., Zhang, W., Xie, W., Tao, P., Chen, C., and Tan, K.: Integrating Temporal Vegetation and Inundation Dynamics for Elevation Mapping Across the Entire Turbid Estuarine Intertidal Zones Using ICESat-2 and Sentinel-2 Data, IEEE J. Sel. Top. Appl. Earth Obs. Remote Sens., 18, 14517-14534, https://doi.org/10.1109/JSTARS.2025.3571791, 2025.

Ye, M., Yang, C., Zhang, X., Li, S., Peng, X., Li, Y., and Chen, T.: Shallow Water Bathymetry Inversion Based on Machine Learning Using ICESat-2 and Sentinel-2 Data, Remote Sens., 16, https://doi.org/10.3390/rs16234603, 2024.

Zhang, S., Xu, N., Zhang, R., Xing, J., and Xiao, X.: Global-scale analysis of coastline expansion in the era of rising sea levels, J. Oper. Oceanogr., 18, 164-182, https://doi.org/10.1080/1755876X.2025.2531716, 2025.

Zhang, W., Xu, Y., Hoitink, A. J. F., Sassi, M. G., Zheng, J., Chen, X., and Zhang, C.: Morphological change in the Pearl River Delta, China, Mar. Geol., 363, 202-219, https://doi.org/10.1016/j.margeo.2015.02.012, 2015.

Zhang, Z., Xu, N., Li, Y., and Li, Y.: Sub-continental-scale mapping of tidal wetland composition for East Asia: A novel algorithm integrating satellite tide-level and phenological features, Remote Sens. Environ., 269, 112799, https://doi.org/10.1016/j.rse.2021.112799, 2022.

Zhao, C., Qin, C.-Z., and Teng, J.: Mapping large-area tidal flats without the dependence on tidal elevations: A case study of Southern China, ISPRS J. Photogramm. Remote Sens., 159, 256-270, https://doi.org/10.1016/j.isprsjprs.2019.11.022, 2020.